Sorbjan, Z. (2003) *Air-Pollution Meteorology*. Chapter 4 of *AIR QUALITY MODELING - Theories, Methodologies, Computational Techniques, and Available Databases and Software. Vol. I - Fundamentals* (P. Zannetti, Editor). Published by The EnviroComp Institute (http://www.envirocomp.org/) and the Air & Waste Management Association (http://www.awma.org/).

Chapter 4

Air Pollution Meteorology

Zbigniew Sorbjan

Department of Physics, Marquette University, Milwaukee, WI 53201, USA
sorbjanz@mu.edu

Abstract: The primary object of this chapter is to introduce meteorological fundamentals related to the transport of air pollutants in the atmosphere. The material contained in the chapter is divided into two sections. Section 1 is very basic and mostly related to atmospheric flows in larger scales. It discusses forms of atmospheric motions, weather systems, forces, and clouds. The material contained in Section 2 is more detailed and focused on processes in the atmospheric boundary layer. Turbulence, mixing and diffusion in this layer are examined and explained. Various regimes, such as stable flows, free and forced convection, in cloud-less and cloud-topped mixed layers are discussed. Their mathematical and physical description is also reviewed, including similarity theories and mixed layer models.

Key words: atmospheric motions, weather systems, atmospheric boundary layer, turbulence, mixing, diffusion, convection, mixed layers, similarity theories**.**

Meteorology has an important, practical application in the area of control and management of air quality. Its significance was first realized when the increasingly heavy use of coal for home heating and industrial power led to episodes of extreme sulfur pollution during certain weather conditions. The most famous case occurred in London during foggy December in 1952, when approximately 4000 people died as the direct result of air pollution. Four years later, in January 1956, under similar conditions, 1000 deaths were blamed on an extended fog in London. Since that time, the problem has grown as a result of industrialization. High air pollution concentrations are no longer local and restricted to urban areas, but can be transported for long distances by large-scale weather patterns.

© EnviroComp Institute and Air & Waste Management Association

The primary object of this chapter is to introduce meteorological fundamentals related to the transport of air pollutants in the atmosphere. The material contained in Section 1 is very basic and mostly related to atmospheric flows in larger scales. More extensive coverage of topics included in this Section can be found in such text-books as Aguada and Burt (2001), Moran and Morgan (1995) or Lutgens and Tarbuck (1995). Readers who are familiar with general meteorology could simply skip it and begin with Section 2.

The material contained in Section 2 is more detailed and describes meteorological processes in the atmospheric boundary layer, where most human and biological activities take place. For further information on boundary layer processes, the reader is referenced to text-books on the subject, including monographs of Kaimal and Finnigan (1994), Garratt (1992), Plate et al. (1998), Sorbjan (1989), or Stull (1988). Air pollution diffusion is investigated in detail by Arya (1999), Venkatram and Wyngaard (1988), or Pasquill (1974).

1 Synoptic Meteorology

1.1 Atmospheric Air

Photographs taken from outer space show that the Earth's atmosphere forms a very thin layer surrounding the globe. Its height can be estimated to be about 80 km, which is 1.25% of the Earth's radius. The composition of the atmosphere is almost uniform with height. Table 1 shows the abundance of the various gases in the atmosphere. The gases listed in the left column of the table are permanent, i.e., their concentrations do not change in time and space. The gases in the other column can vary.

Table 1. Abundance of the atmospheric gases

Permanent Gas	Symbol	% by Variable	Gas	Symbol	% by Volume
Nitrogen	N_2	78.08	Water vapor	H_2O	0.0 – 4.0
Oxygen	O_2	20.95	Carbon dioxide	CO_2	0.0351
Argon	Ar	0.93	Methane	CH_4	0.00017
Neon	Ne	0.0018	Carbon monoxide	CO	0.00002
Helium	He	0.00052	Ozone	O_3	0.000004
Hydrogen	H_2	0.00005	Sulfur dioxide	SO_2	0.000001
Xenon	Xe	0.000009	Nitrogen dioxide	NO_2	0.000001

Nitrogen and oxygen are the most abundant atmospheric gases. Their total amount is about 99.03%. The abundance of the remaining permanent gases is only about 0.9324%. The concentration of water vapor, which is also one of the variable atmospheric gases, changes as a part of the natural hydrologic cycle. The concentration of the carbon dioxide (CO_2) and methane (CH_4) show cyclic

oscillations associated with the annual vegetation cycle (see website[1]). The amount of sulfur dioxide (SO_2) may vary due to volcanic eruptions into the upper atmosphere and also due to anthropogenic activities.

Most of the ozone is found in the higher atmosphere, about 30 km above the Earth's surface. At this height, ozone is produced naturally and forms the so-called ozone layer. The ozone layer absorbs most of the ultraviolet radiation from the sun. Ultraviolet radiation is harmful to life. Therefore, the presence of the ozone layer in the atmosphere protects life on Earth against radiation.

In 1974, M.Molina, F.S.Rowland and P.Crutzen, determined that certain man-made substances have been destroying the ozone layer. Among these substances were chloro-fluoro-carbons (CFCs) from spray cans and air-conditioning systems. When released into the atmosphere, CFCs slowly move upwards. In the upper atmosphere they are transported to remote regions including the Arctic and Antarctic. During this transport CFCs break up as a result of solar radiation. Chlorine molecules are produced which react with ozone and reduce its amount. Evidence of massive ozone layer destruction, called the ozone hole (see website[2]), has been observed over Antarctica. As a consequence, an increase in skin cancer in humans may be expected, as well as various adverse effects on plants and animals. To solve the ozone reduction problem, over forty industrialized countries in the world have pledged to eliminate completely the use of ozone-depleting chemicals in the 21st century.

Some of the variable atmospheric gases in the atmosphere change their amounts as a result of anthropogenic industrial activities. For example, ozone (O_3), nitrogen dioxide (NO_2), and carbon monoxide (CO) are emitted into the lower atmosphere by motor vehicles, due to the high-temperature combustion of fuel. Ozone is also formed as a result of photochemical reactions. Carbon dioxide (CO_2) and sulfur dioxide (SO_2) are produced by burning wood and coal. Sulfur dioxide readily oxidizes to sulfur trioxide (SO_3). In moist air, sulfur trioxide reacts with water and produces sulfuric acid (H_2SO_4). Sulfuric acid can be transported within clouds for hundreds of kilometers. When it is removed from the clouds, it can result in acid rain.

1.2 Atmospheric Energy

The Earth's atmosphere acts as a giant heat engine transforming available energy into the movement of huge masses of air. Practically all "fuel" for this engine is supplied by the sun. The contribution of all other sources (e.g. the Earth's interior) is smaller than 0.02%. Since the Earth's atmosphere is semi-transparent to incoming solar radiation, it obtains roughly 20% of its energy strictly by

[1] http://www.oism.org/pproject/s33p36.htm
[2] http://www.epa.gov/ozone/science/hole/

absorption. About 30% of solar radiation is reflected or scattered into space. The rest passes through the atmosphere and is absorbed by the Earth's surface.

The surface of the Earth has a considerable influence on air temperature. Differences in temperature near the ground are caused by the variation of thermal properties of the underlying surface. Because water has an enormous specific heat, it takes far more heat to raise the temperature of water than it does to raise the temperature of rocks or soil. Besides, the heating energy is deposited only in a few decimeters of soil, while in the oceans it is mixed through the top few meters of water. Consequently, since water covers 61% of the Northern Hemisphere and 81% of the Southern Hemisphere, there are considerably smaller annual temperature variations in the water-dominated Southern Hemisphere, as compared to the Northern one.

Temperature in the atmosphere changes with height. In the troposphere, which is the lowest layer of the atmosphere -- extending up to about 10 km above the ground, the temperature in average decreases with height at the rate of about 0.6^{o}C per 100 m (Figure 1). Above, in the stratosphere, temperature generally increases with height, due to an absorption of solar radiation in the ozone layer. In the mesosphere, temperature decreases with height. In the thermosphere, the temperature of air molecules again increases with height. Departures from the plot in the figure can occur because of seasonal and latitudinal variations.

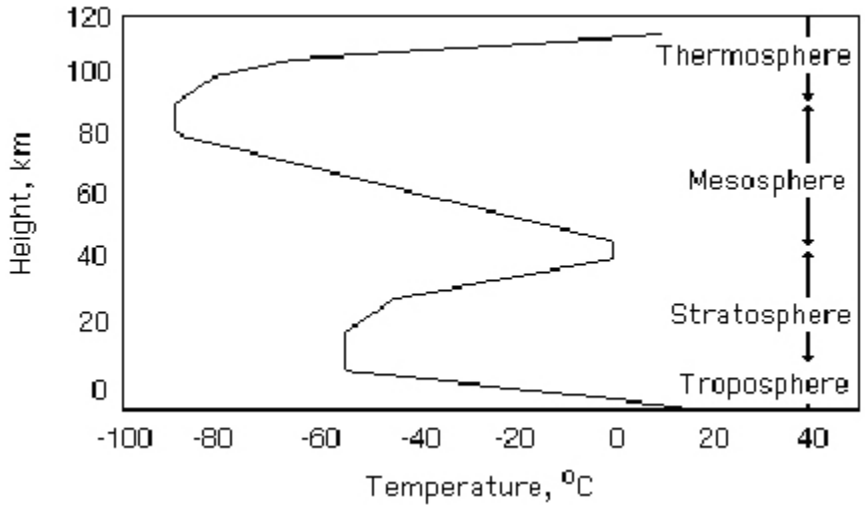

Figure 1. The vertical distribution of temperature in the standard atmosphere.

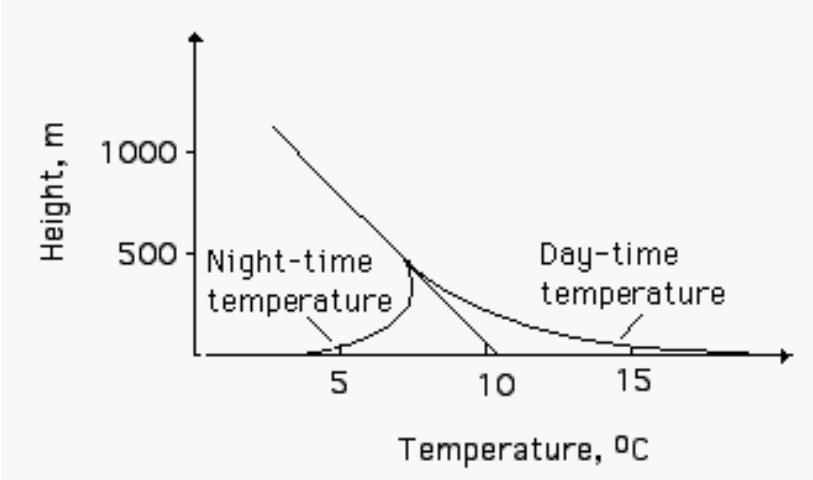

Figure 2. Typical temporal changes of temperature within the first few hundred meters above the Earth's surface.

Within the first few hundred meters, temperature significantly changes diurnally (Figure 2). At night, the Earth's surface cools radiatively and causes a decrease in air temperature near the surface. As a result, the so-called temperature inversion layer is formed near the Earth's surface. In the inversion layer, the temperature increases with height. On the other hand, during the day, the Earth's surface is heated by the sun. The warm surface causes an increase of the air temperature in a thin layer above the ground. As a result, the daytime air temperature near the ground readily decreases with height.

Temporal variations of the air temperature in the atmosphere can also be related to various natural, and anthropogenic factors, such as volcanic eruptions and increased levels of air pollutants. During volcanic eruptions, tons of dust and ash are spewed into the atmosphere. Some of this material reaches the levels above the troposphere and is redistributed around the Earth. The temporary presence of volcanic debris causes some of the sun's energy to be reflected back into outer space before it reaches the Earth's surface. Volcanic particles also intensify cloud formation. More clouds reflect more solar energy back into outer space. Even though the volcanic dust and clouds also prevent some of the Earth's heat from escaping, the resulting effect is a cooling of the Earth.

There has been concern that further industrial emissions of pollutants into the atmosphere will cause global warming, commonly referred to as the greenhouse effect. The greenhouse effect is triggered by such pollutants as carbon dioxide, methane, nitrous oxide, and chloro-fluoro-carbons. Greenhouse gases prevent part of the Earth's radiation from escaping into space, and keep the Earth warmer. A globally averaged surface temperature increase of 0.5°C has already been observed since 1880 (see web site[3]). As a result of the warming effects, glacier and continental ice could melt, resulting in rising sea levels. More water vapor

[3] http://lwf.ncdc.noaa.gov/img/climate/research/1998/anomalies/triad_pg.gif

could be released into the air causing greater precipitation. A weakening of the Gulf Stream current might also occur. The warming trend could shift climate zones around the world and make floods, droughts, storms, cold and heat waves to be more extreme and more frequent.

There is some skepticism in the scientific community about such an "apocalyptic" vision of the future. The observed 0.5^{o}C temperature increase could merely be a natural climate fluctuation. Global warming caused by the greenhouse effect could be canceled due to radiative cooling by the increased presence of anthropogenic aerosols and clouds. Reduction of the ozone content, and consequently in the amount of the absorbed solar energy, is expected to cool the stratosphere.

Nonetheless, the recent model simulations imply that only about 3.3% of the greenhouse energy is used to warm the atmosphere. Most of this energy (92%) is stored in the oceans. In addition, about 4.1% of the greenhouse energy causes the melting of the ice cover in Antarctica and Greenland, and about 0.5% melts the world glaciers.

1.3 Atmospheric Forces

Atmospheric motion results from the action of atmospheric forces. Such forces may be classified into two categories -- body forces and surface forces. Body forces, such as gravity, act at a distance on the bulk of the air parcel (hence the word "body"). Surface forces, or stresses (forces per unit area), act through direct contact and are exerted directly on the surface of the air parcel. The surface forces can be divided into normal stresses and tangential (shear) stresses.

Surface forces reflect an interaction among air molecules or air parcels. If two layers of air flow with slightly different velocities, the random sidewise intrusions of some slower molecules into the faster stream tend to slow down the faster stream. The intrusion of faster molecules into the slower stream tend to speed up the slower stream. The wandering of individual molecules introduces internal friction in the fluid which is called viscosity.

The atmospheric pressure can be regarded as the weight of the atmosphere per unit area. Pressure differences in space generate the pressure gradient force which acts from higher to lower pressure regions of the atmosphere. As the atmospheric pressure decreases with height, one might expect that the vertical component of the pressure force should be able to move the atmospheric air out into space. But this does not occur because the vertical pressure gradient force is approximately balanced by the gravity force. This balance is expressed by the hydrostatic equation, which can be written in the following form:

$$-\frac{1}{\rho}\frac{dp}{dz} = g \tag{1}$$

where z is height, ρ is the air density, p is the air pressure, g is the gravity acceleration. The hydrostatic balance may be disturbed by the buoyancy force, due to density differences between parcels of moving air and their vicinity, as well as by varying motions in time and space.

Buoyancy forces act on individual parcels of air only when there are differences in density between the parcels and the ambient atmospheric air. For instance, the buoyancy force appears when a number of water vapor molecules is added to a fixed volume of air. In this case the same number of air molecules must leave this volume to keep the total number of molecules (Avogadro's law), as well as temperature and pressure constant. Assume that 10 moles (1 mole is a fixed number of molecules) of water vapor replace 10 moles of air, i.e., 8 moles of nitrogen and 2 moles of oxygen. The molecular weights of water vapor, nitrogen, and oxygen are: 18 g, 28 g, and 32 g, respectively. Therefore, the atomic weight budget is: *(10 x 18 g) - (8 x 28 g + 2 x 32) = -108 g (lost)*. This indicates that humid air is lighter than dry air of the same temperature and pressure. Other effects of the buoyancy force will be discussed in the next section.

The rotation of the Earth introduces the Coriolis force. The Coriolis force is perpendicular to the object's relative velocity, and is oriented to the right of the velocity vector in the northern hemisphere, and to the left in the southern one. Its magnitude is proportional to the product of an object's mass, its velocity, Earth's angular velocity (7.29×10^{-5} radians/s), and sin ϕ, where ϕ is the latitude at which wind occurs.

The Coriolis effect combines two factors, one that exerts its strongest force on objects traveling on a north-south axis, and another which affects objects moving on an east-west axis. The first factor results from the rotational velocity of the Earth's surface, which varies with latitude. A point residing on the Equator moves at a speed of $2\pi R/24h = 463.2$ *m/s*, while the poles spin but do not move. Hence, air moving north from the Equator begins with a greater rotational speed and outruns slower moving portions of the globe. As a result, it relatively curves eastward and ahead of the Earth's rotation. Similarly, air traveling southward, toward the Equator, begins with a low initial velocity and curves west, as the faster-moving Earth exceeds it.

The east-west component of the Coriolis force is a consequence of the tendency of any orbiting object to fly off in a straight line. This tendency, together with the rotation of the Earth, produces a force which lies on the plane perpendicular to the Earth's axis, and thus has a sideways component in relation to the Earth's surface. Consequently, an object moving east will curve toward the Equator, while an object moving westward will curve toward the pole.

1.4 Static Stability

The buoyancy force can also appear when air parcels travel vertically in the atmosphere. A dry parcel of air moving upward expands adiabatically due to a decrease in the atmospheric pressure with height (the word adiabatic is derived from the Greek word adiabatos, meaning "impassible", i.e., occurring without loss or gain of heat). The process of expansion decreases the internal energy of parcel molecules, and causes the parcel to cool. When a dry parcel of air moves downwards, it contracts adiabatically due to an increase in the atmospheric pressure with height. The process of contraction increases the internal energy of parcel molecules, and causes the parcel to warm. Changes of the temperature in a dry adiabatic process are described by the Poisson equation:

$$\frac{T(z)}{T_o} = \left\{ \frac{p(z)}{p_o} \right\}^k \tag{2}$$

where T is the absolute temperature in Kelvins, p is pressure, $k = R/c_p = 0.286$, R is the gas constant of dry air ($R = 287\ m^2 s^{-2} K^{-1}$), c_p is the specific heat of dry air ($c_p = 1007\ m^2 s^{-2} K^{-1}$), z is the actual height and "o" indicates the initial level of the moving parcel.

Differentiating the above equation, with respect to height, with the help of the hydrostatic equation (1), and the equation of state:

$$p = \rho R T \tag{3}$$

which relates the pressure, temperature and density, one finds that the temperature of a vertically moving parcel changes in the atmosphere at the constant lapse rate $\gamma_a = -\ dT/dz = g/c_p \approx 1^o C$ *per 100 m.* This value is called the dry adiabatic lapse rate (the lapse rate is defined as a negative vertical gradient).

If the atmosphere were well mixed by vertical motions of air parcels, its temperature would not be constant but would decrease with height at the dry adiabatic lapse rate. In the well mixed atmosphere the so-called potential temperature would be constant. The potential temperature is defined as:

$$\Theta = T(z) \left\{ \frac{1000}{p(z)} \right\}^k \tag{4}$$

i.e., it is the temperature of a parcel which is brought adiabatically to the reference level of 1000 hPa. Note that the pressure p in (4) is expressed in hPa. By differentiating (4) with respect to height, with the help of (1), one can obtain $d\Theta/dz = dT/dz + \gamma_a$. This indicates that the potential temperature is indeed conserved (constant) during vertical adiabatic motions.

Condensation of water vapor has an important impact on the state of the atmosphere. When the rising parcel of air reaches saturation, vapor condenses and releases the latent heat of condensation. The released heat increases the air parcel's temperature. As a result, the adiabatic lapse rate decreases from the dry rate of $\gamma_a = 1^oC/100\ m$ to the rate $\gamma_m = \gamma_a - L/c_p\ dq/dz$, where L is the latent heat of evaporation ($L = 2.5x10^6\ J/kg\ at\ 0^oC$), q is the specific humidity (mass of water vapor in a kilogram of humid air). The new rate is called the pseudo-adiabatic lapse rate or the moist adiabatic lapse rate. The moist adiabatic lapse rate for the standard atmosphere varies from 0.4°C/100 m (in warm saturated air) to 0.9°C/100 m (in cold saturated air). The release of latent heat causes the rising parcel to intensify its vertical motion. This mechanism provides additional "fuel" for the formation of thunderstorms.

The actual temperature lapse rate in the atmosphere varies in time and space and usually differs from the dry adiabatic rate. Therefore, in some situations, the rising parcel of air might be cooler, and thus heavier, than the surrounding air. Such a parcel is decelerated in its upward motion, and then forced to sink. Such a case is considered in Figure 3.

The ambient temperature in the figure increases with height from T_1 = 300 K to T_2 = 301 K. A parcel, which initially has a temperature of T_{p1} = 300 K, is forced upwards. As a result, it expands and cools adiabatically to T_{p2} = 299 K. Being cooler and heavier than the ambient air, the parcel would tend to return to the initial level. When this occurs, the conditions are called statically stable.

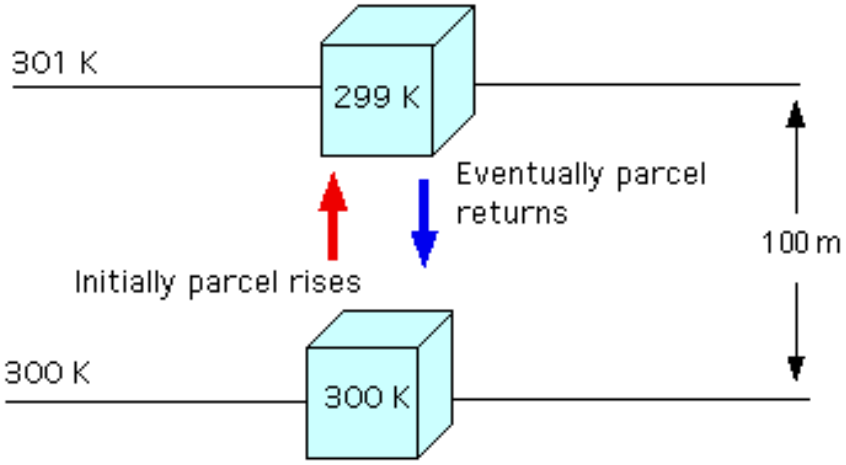

Figure 3. Static stability within thermal inversion (i.e., when the temperature of the atmosphere increases with height). The temperature is expressed in Kelvins.

If the temperature of the ambient air in the figure decreased with height from T_1 = 300 K to T_2 = 298 K, the rising air at the upper level would be warmer (T_{p2} = 299 K), and therefore lighter, than the surrounding air (T_2 = 298 K). As a result, the parcel would continue rising. Consequently, this state would be called statically

unstable. In the statically neutral case, the rising particle has the same temperature along its path as the surrounding air ($T_1 = T_{p1}$, $T_2 = T_{p2}$).

To further understand the effects of thermal stability, consider the balance of the gravity and the pressure gradient forces given by Equation (1). It can be assumed that one parcel of air changes its density from the value ρ to a new value $\tilde{\rho}$. As a result of this change, the parcel starts moving vertically with the acceleration a:

$$-\frac{1}{\tilde{\rho}}\frac{dp}{dz} = g + a \tag{5}$$

Substituting (1) into(5) and employing the equation of state (3) yields:

$$a = -g\left(\frac{\tilde{\rho}-\rho}{\tilde{\rho}}\right) = -g\left(\frac{T-\tilde{T}}{T}\right) = -\frac{g}{T}\left(\frac{dT}{dz} - \frac{d\tilde{T}}{dz}\right)z = -\frac{g}{T}\frac{d\Theta}{dz}z \tag{6}$$

where T and $\tilde{T}$ are the temperatures of the atmosphere and the parcel respectively, $-d\tilde{T}/dz = \gamma_a$, Θ is the potential temperature, and z is the height above the Earth's surface.

When $d\Theta/dz > 0$ then $a < 0$. In this case the vertical motion is decelerated. When $d\Theta/dz < 0$ then $a > 0$. In this case the vertical motion is intensified. Based on the above analysis we may conclude that the static stability of the atmosphere can be characterized as follows:

- unstable (superadiabatic): $d\Theta/dz < 0, -dT/dz > \gamma_a$
- neutral (adiabatic): $d\Theta/dz = 0, -dT/dz = \gamma_a$ (7)
- stable (subadiabatic): $d\Theta/dz > 0, -dT/dz < \gamma_a$

and in addition:

- isothermal: $dT/dz = 0, d\Theta/dz = \gamma_a$
- inversion: $dT/dz > 0, d\Theta/dz > \gamma_a$

Equation (6) can be transformed into the form:

$$\frac{d^2z}{dt^2} = -N^2 z \tag{8}$$

where N is the Brunt-Väisälä frequency defined as:

$$N^2 = \frac{g}{T_o}\frac{d\Theta}{dz} \tag{9}$$

The general solution of the differential equation (7) is:

$$z = A\, e^{iNt} + B\, e^{-iNt} \tag{10}$$

If $N^2 > 0$, the stratification is stable and equation (10) describes a vertical oscillation with angular frequency N. The period $2\pi/N$ is typically a few minutes long. These oscillations can be interpreted as gravity waves, since their nature is strongly affected by the action of gravity .

1.5 Scales of Atmospheric Motions

In 1926, L.F. Richardson (1881-1953) noted that atmospheric motion occurs over a broad range of horizontal length scales -- from thousands of kilometers to millimeters. The largest scale motion is caused by thermal and pressure contrasts over the globe, modified by the rotation of the Earth. Land and oceans introduce additional modifications to this primary flow and help to initiate secondary circulations. Local topography introduces tertiary circulations. A cascade process, in which eddies of the largest (global) size trigger smaller and smaller (local) ones, continues down to molecular motions, which finally cease due to viscosity. Richardson's poetic version depicts the changes quite accurately:

> Big whirls have little whirls,
> That feed on their velocity;
> And little whirls have lesser whirls,
> And so on to viscosity.

The range of scales of atmospheric motions can be adequately defined by considering fundamental frequencies of the atmospheric motions (e.g., Atkinson, 1995):

- the Brunt-Vâisâlâ frequency: $N = (g/T_o\, d\Theta/dz)^{1/2} \sim 10^{-2}\ s^{-1}$
- the inertial frequency: $f = 2\Omega \sin\phi \sim 10^{-4}\ s^{-1}$
- the planetary frequency: $P = (U\, b)^{1/2} \sim 10^{-6}\ s^{-1}$

where f is the Coriolis parameter, the Ω angular velocity of the Earth, ϕ is the latitude, U is the horizontal velocity of air, b is the rate at which the Coriolis parameter changes with the latitude. The Brunt-Vâisâlâ frequency N defines gravity oscillations in the stratified atmosphere. The inertial frequency f results from the rotation of the Earth. The planetary frequency P is related to oscillations in the westerlies flow in the middle and upper troposphere.

Based on these fundamental frequencies N, f, and P listed above, the following scales of atmospheric motions can be defined:

- planetary scale: $F < P$, or $F < 10^{-6}\ s$
- large scale: $P < F < f$, or $10^{-6}\ s < F < 10^{-4}\ s$
- meso-scale: $f < F < N$, or $10^{-4}\ s < F < 10^{-2}\ s$
- small scale: $F > N$, or $F > 10^{-2}\ s$

where F is the frequency of the atmospheric circulation under consideration. The corresponding length scale L can be obtained by assuming $L = 2\pi U/F$, where U is the velocity of the air ($U \sim 10$ km/h). Consequently:

- planetary scale: $L > 2\pi U/P$, or $L > 1500$ *km*, but limited by the circumference of the Earth
- large scale: $2\pi U/f < L < 2\pi U/P$, or $200 \text{ km} < L < 1500 \text{ km}$
- meso-scale: $2\pi U/N < L < 2\pi U/f$, or $2 \text{ km} < L < 200 \text{ km}$
- small scale: $L < 2\pi U/N$, or $L < 2$ *km*.

Atmospheric transport and diffusion closely follow this classification. Pollutants from local/urban sources (isolated factories, power plants, waste disposals, e.t.c) are quickly dispersed by small-scale motions near the Earth. Pollutants emitted from major industrial areas or forest fires retain high concentrations for greater distances and are dispersed on small and meso-scales. In cases of powerful sources (e.g., nuclear plant explosions or the burning of oil wells), high concentrations of air pollution can remain in the atmosphere for a very long time.

The planetary scale circulations transport material injected into higher levels of the atmosphere. Such injections can occur during volcanic eruptions, when tons of dust and ash are spewed into the atmosphere. Some of this material reaches to the levels of the stratosphere and can be slowly redistributed around the Earth by planetary-scale circulations. Pollutants which do not reach above the troposphere are dispersed much faster by large, meso- and small-scales motions. A more detailed discussion of atmospheric motions of various scales is introduced in the following sections.

1.6 Planetary-Scale Circulations

The planetary-scale circulation of the atmosphere is schematically illustrated in Figure 4. An understanding of planetary-scale circulations is necessary to an appropriate description of tropospheric and stratospheric transport and transformations of carbon dioxide, methane, ozone, water vapor, nitrous oxide, chloro-fluoro-carbons, and aerosols. For this reason the analysis of planetary-scale circulations is often performed in conjunction with atmospheric chemistry. This approach was used, for example, to explain the ozone-hole effect.

As depicted in Figure 4, at the equator (latitude 0^o) air is thermally forced upward and begins its high-level flow to the north and to the south. At the same time, the air over the north pole begins its low-level journey southward. This simple convective transfer between the equator and the poles is disrupted by the Earth's rotation, and three separate circulation cells are established. The subtropical cell is called the Hadley cell, the middle one is called the Ferrel cell, and the third one is called the Polar cell.

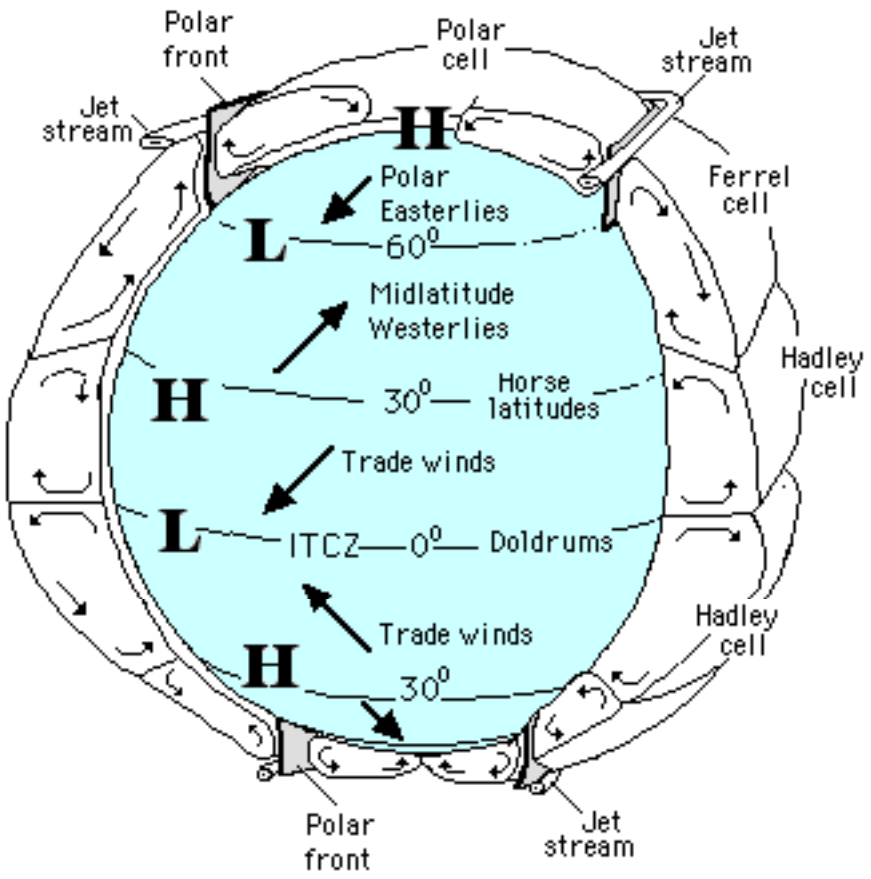

Figure 4. The general circulation of the atmosphere. Idealized zonal belts of high and low pressure systems are marked by letters H and L.

In the northern hemisphere, the Coriolis force turns the air to the right. As a result, below the 30° latitude, lower winds become easterly and upper winds westerly. At the same time, the air over the north pole is deflected to the right, and becomes easterly above 60 ° latitude. A similar picture occurs in the southern hemisphere.

A semi-permanent high pressure belt (marked by a letter H) is formed near the 30° latitude, in both the northern and southern hemispheres. Air ascends around 60° latitude in subpolar low pressure zones (marked by a letter L), which are created in both hemispheres. Subpolar lows are accompanied by a distinct boundary, which separates cold air moving south, and mild air traveling poleward. This boundary between the Polar and Ferrel cells is called the "polar front". In the tropopause, above the Polar front, there is a meandering globe-circling current of westerly winds. The current, called a "jet-stream", moves air with a typical speed of about 150 km/h. It is hundreds of kilometers wide and only a few kilometers deep (see its photo at web site[4]).

[4] http://www.lpi.usra.edu/images/sclo/sclo_S02.gif

A zone near the equator is called the "intertropical convergence zone" (ITCZ, see web site[5]). This region of very monotonous weather and weak winds is referred to as the "doldrums". Steady east winds in the zone 0^o to 30^o are called the “trade winds”. Trade winds provided sailing ships with a route from Europe to America. From the 16th to the 19th centuries, the northeast trades were used to transport goods to Africa, where they were exchanged for slaves. From Africa, sailing boats filled with human cargo voyaged to America, employing southeast trades. From America, with the help of prevailing westerlies, they returned to Europe loaded with sugar, rum and cotton.

Latitudes of about 30^o are called the "horse latitudes". In this specific region, sailing was frequently very slow and when food dwindled, horses were eaten by the sailors.

1.7 Large-Scale Circulations

Large-scale circulations are characterized by horizontal length scales varying from few hundreds to few thousands kilometers. Such circulations affect mostly horizontal dispersion of pollutants in the troposphere on time scales of days to several weeks. Large-scale circulations in the atmosphere are dependent on distribution of pressure patterns. Five distinct pressure systems can be defined surface weather charts (see Figure 5):

1. Lows (marked by a letter L), also called cyclones, pressure systems surrounded on all sides by higher pressure;
2. Highs (marked by a letter H), also called anticyclones, pressure systems surrounded on all sides by lower pressure;
3. Troughs, elongated areas of low pressure with the lowest pressure along a line marking the maximum curvature of isobars;
4. Ridges, elongated areas of high pressure with the highest pressure along a line marking the maximum curvature; and
5. Cols, neutral areas between two lows and two highs.

Large-scale circulations transport various air masses. Atmospheric air masses are bodies of air with nearly uniform temperature and moisture. Air masses can be classified depending upon their source regions as polar (P), arctic (A), or tropical (T). Each of those masses can also be specified as continental (c), or marine (m). Moreover, a small letter (w) or (k) was used to indicate that an air mass was warmer or cooler than the underlying surface. Therefore, "mTw" would indicate hot and humid tropical air initiated over the ocean and warmer than the underlying surface.

[5] http://www.cyf-kr.edu.pl/IMGW/sat/index_pl.html

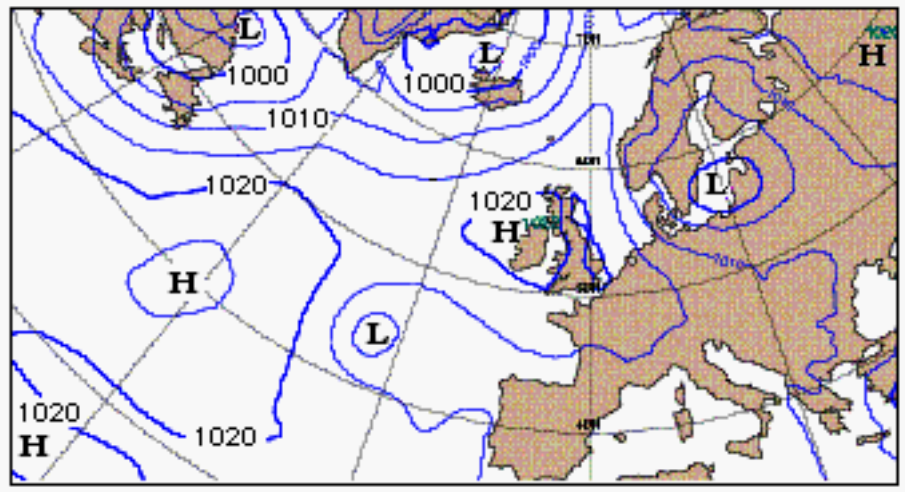

Figure 5. A typical surface weather chart.

A transition zone between two different air masses is called a front (see the photo on the web site[6]). Fronts form at outer boundaries of high-pressure systems and extend all the way to the center of the low-pressure system (Figure 6). Across the frontal zone, temperature, humidity and wind often change rapidly over short distances. Fronts can be classified into four groups: cold, warm, occluded and stationary. The cold front is the leading edge of an advancing cold air mass. Analogously, the leading edge of an advancing warm air mass is called the warm front. When the cold front catches up with the warm front, the two occlude (close together). The result is an occluded front. When neither the cold nor warm air masses are advancing, the front is called stationary.

At the cold front, colder and denser air wedges under the warmer air and forces it upward. The frontal edge has an average slope of 1:50 (1 unit of height: 50 units of length), which is due to friction which slows the flow near the ground. As the moist, unstable air rises, its water vapor condenses into a series of cumulus clouds, cumulonimbus (Cb), and altocumulus (Ac). Strong, upper level winds blow the cirrostratus (Cs) and cirrus (Ci) clouds, far in advance of the approaching front, as shown in the Figure 7.

[6] http://www.photolib.noaa.gov/historic/nws/wea00025.htm

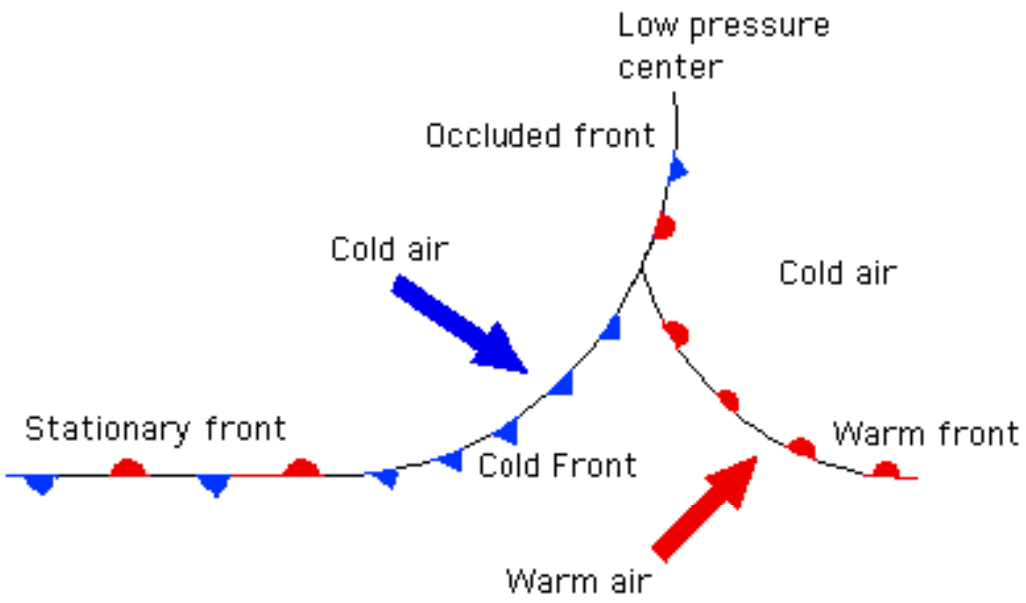

Figure 6. Atmospheric fronts on a surface weather chart.

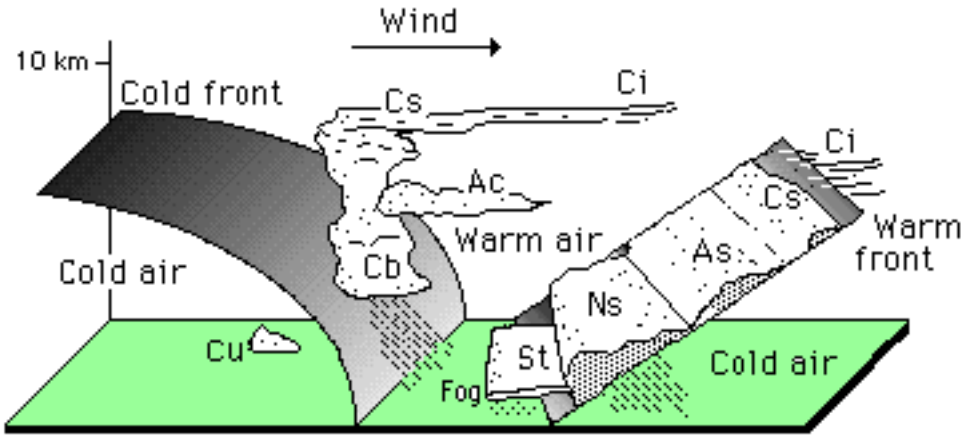

Figure 7. Frontal cloud systems.

The frontal surface of the warm front is less steep (about 1:100). Behind a warm front the stratus clouds (St) and fog are observed near the Earth's surface. Stratus clouds can produce drizzle. As air moves upward along the warm front, nimbostratus clouds (Ns) form, producing a broad area of rain or snow. Farther along the front, clouds gradually transform into altostratus (As), and then into a thin, white veil of cirrostratus (Cs). On top of the frontal surface, there are usually cirrus (Ci) clouds.

There is a simple empirical rule, known as the Buys-Ballot law, which relates the direction of the wind near the Earth's surface to the pressure field. The rule is strictly valid above the near-surface layer of frictional influence. According to the

Buys-Ballot law, if you stand in the Northern Hemisphere, with the wind blowing at your back, the low pressure center will be located to the left. In the southern hemisphere, with the wind blowing at your back, the low pressure will be located to the right. The explanation of the rule is shown in Figure 8.

When the air mass is pushed by the horizontal pressure gradient force, it initially moves towards the low pressure area (vector V_1 in the figure). The moving parcel is simultaneously under the influence of the Coriolis force (outlined arrows indicated as C_1 and C_2), which changes its direction (vectors V_2 and V_3). The air changes its direction until an equilibrium between the pressure and the Coriolis forces is reached. The wind resulting from this equilibrium blows along isobars (lines in the figure marked 1000 mb, 1004 mb), and is called geostrophic. The term was coined from the Greek words: ge, "the Earth", and strophein, "to turn".

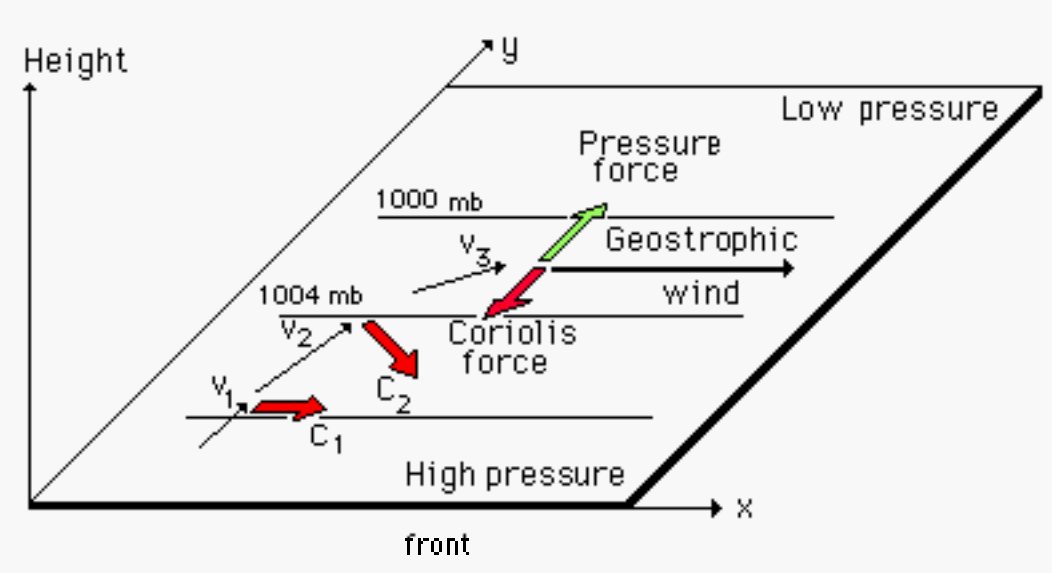

Figure 8. The geostrophic wind on the surface weather chart.

The isobars in Figure 8 are straight lines. In cases with strongly curved isobars, there is a balance of the pressure gradient, Coriolis, and the centrifugal forces (centri: center, fugio: to flee). In the Northern Hemisphere this balance is associated with a clockwise circulation in anticyclonic (high) pressure systems, and counterclockwise circulation in cyclonic (low pressure) ones (Figure 9a).

Near the Earth's surface, in the presence of friction, the pressure force is no longer balanced by the Coriolis and centrifugal forces, and the wind is directed from high pressure to low pressure, crossing isobars at an angle of about 30^o (Figure 9b). The resulting inward motion toward a low pressure center is called horizontal convergence. In just the opposite, outflow in a high pressure center is called horizontal divergence. Horizontal convergence near the ground in the low-pressure system causes the accumulation of air in the center. To remove inward-flowing air, a very slow (a few cm/s) but persistent vertical upward motion is

generated. On the other hand, there is a descending flow of air to compensate for the high-pressure divergence near the ground.

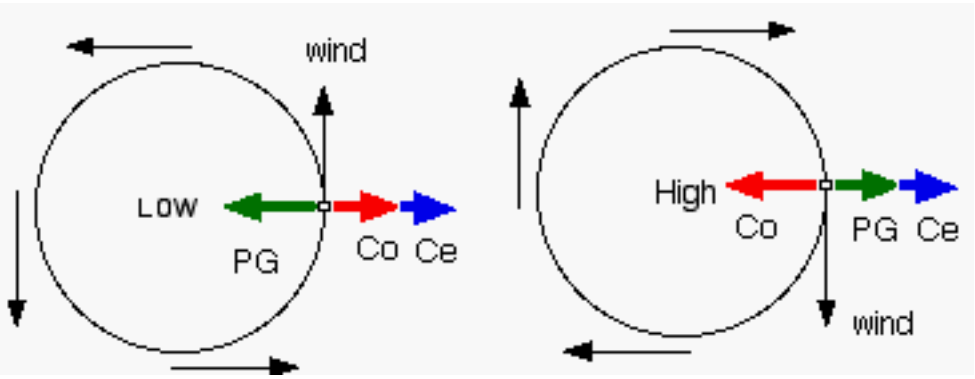

Figure 9a. Flow in the pressure systems without friction (upper row) near the Earth's surface. PG-the pressure gradient force, Co-the Coriolis force, Ce-the centripetal force

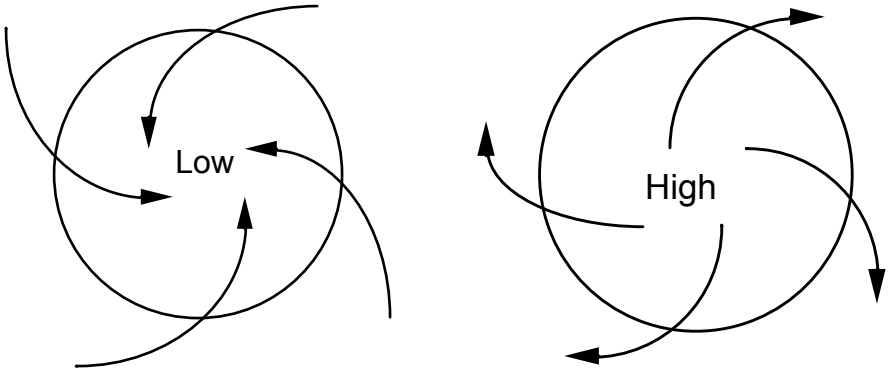

Figure 9b. Flow in the pressure systems with friction near the Earth's surface. PG-the pressure gradient force, Co-the Coriolis force, Ce-the centripetal force.

Because most fluid phenomena on the Earth involve rotation, the concept of vorticity is useful to explain complex atmospheric motions. Vorticity occurs as a result of different portions of fluid being moved by different amounts. To define vorticity, a cross-like element "+" between two mutually perpendicular infinitesimal fluid lines can be considered. The sum of their angular velocities (around an axis which is perpendicular to the plane of the cross "+") is called vorticity (around this axis). In laboratory conditions, vorticity (around an axis) can be measured by a simple vorticity-meter, which consists of four vanes rigidly attached at right angles to a vertical axis.

Vorticity is a vector quantity, since it depends on the orientation of the axis of rotation. In meteorology, rotation about a vertical axis is often considered. Vorticity is defined to be positive (cyclonic) when the fluid spins counter-

clockwise, and negative (anticyclonic) when the fluid spins clockwise (when viewed from above). Because the Earth spins, it also has vorticity. In the northern hemisphere, the Earth's vorticity is always positive, because the Earth spins counter-clockwise about its vertical axis.

The amount of the Earth's vorticity depends on latitude. If the vorticity-meter is placed on the north pole, it will spin about its vertical axis, with the speed of one revolution per day. Thus, according to our definition, the Earth's vorticity equals the doubled angular velocity of the Earth. When the vorticity-meter is placed on the equator, it will not spin about its vertical axis. Its vorticity is nil. The absolute vorticity is defined as a sum of the Earth's vorticity and the vorticity of the air relative to the Earth.

The concept of vorticity is useful for explaining many phenomena in the atmosphere. For instance, it can be used to explain the development of Rossby waves in westerlies flow (Figure 10), in the middle and upper troposphere. Rossby waves are wavelike patterns, usually three to five in number, which extend completely around the Earth. The wave flow of the westerlies provides an important mechanism for heat and contaminant transfer across mid-latitudes.

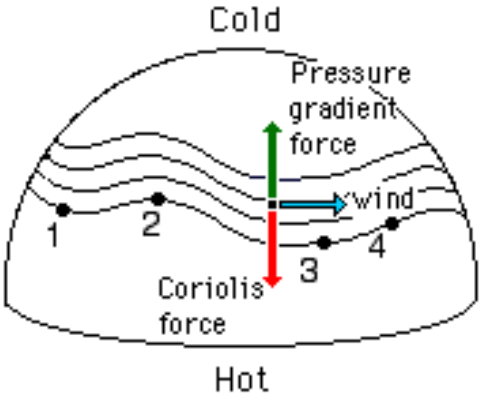

Figure 10. Rossby waves: wave-like patterns in westerlies flow.

Westerlies depicted in Figure 10 exist as a result of a balance between the horizontal pressure gradient and Coriolis forces. To explain Rossby waves consider a parcel of air in the middle troposphere (about 5 km above the Earth) at position "1". It has been proven that such a parcel conserves its absolute vorticity. Imagine that the parcel is heading toward the pole, to the region of increasing Earth's vorticity. To keep the absolute vorticity constant, there must be a corresponding decrease in the relative vorticity of the parcel. Consequently, at position "2", the parcel turns clockwise toward the southeast. Now the air is moving into a region where the Earth's vorticity is smaller. As a result, the parcel's relative vorticity must increase. At position "3", the air turns counterclockwise, and at position "4" begins to head toward the Pole again.

1.8 Meso-Scale Circulations

Meso-scale circulations can be characterized by horizontal length scales on the order of a few tens to several hundred kilometers. Meso-scale flows can be mechanically or thermally forced and generated near the Earth's surface due to the effects of the Earth's topography, or in the free-atmosphere. For example, up-slope or down-slope winds are circulations which are mechanically forced by topography. Examples of circulations, which are thermally forced in the free atmosphere, include hurricanes, (see photo at web site[7]), severe convective storms. (see web site [8]), and frontal circulations. Gravity waves are circulations which are dynamically or thermally forced by topography (see the web site[9]).

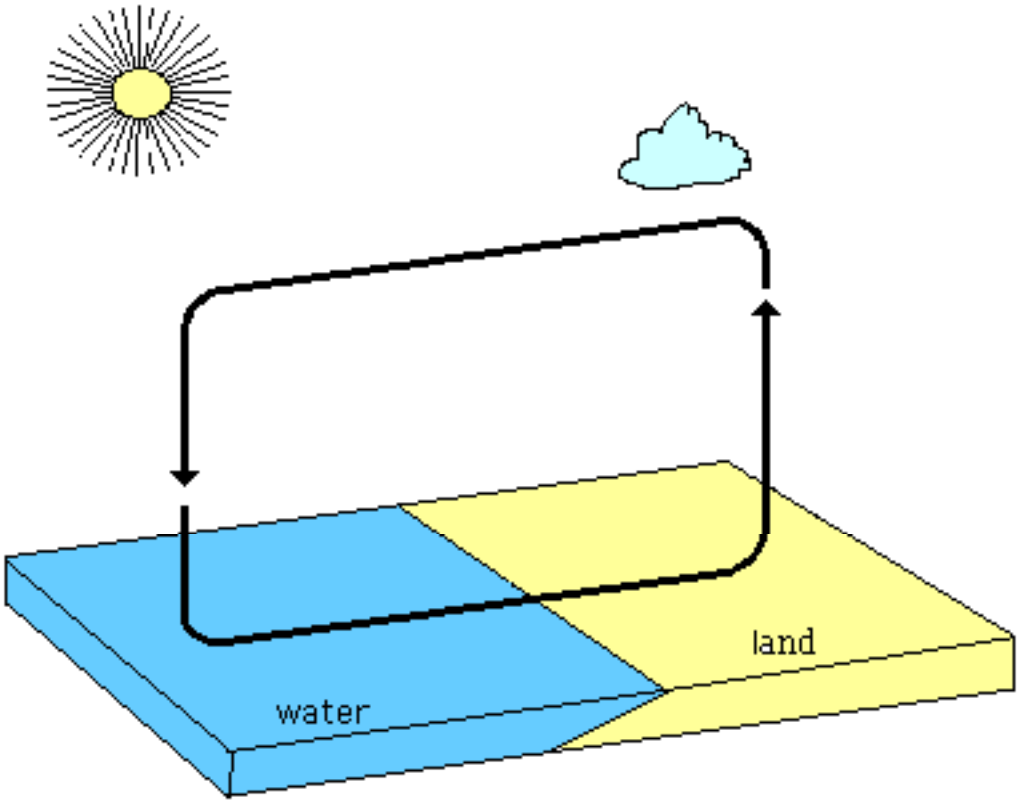

Figure 11. A schematic structure of the sea breeze.

Meso-scale convection is often induced by the temperature contrasts at the Earth's surface. Resulting circulations include sea/land breezes, lake breezes, urban heat islands, mountain and valley winds, and monsoons. They are best developed when large-scale winds are weak. One example is the sea/land breeze generated by the diurnal differences of temperature between the sea and the land. During the daytime, the coast heats more rapidly than the sea, which causes convection

[7] http://www.lpi.usra.edu/images/sclo/sclo_S30.gif
[8] http://www.lpi.usra.edu/images/sclo/sclo_S05.gif
[9] http://www.lpi.usra.edu/images/sclo/sclo_S20.gif

over hot land. Conversely, at night, land cools more quickly than the sea, which causes subsidence of air (Figure 11). As a result, the compensating flow during the day (sea breeze) is directed toward the land, and in the opposite direction at night (land breeze).

Traces of meso-scale flows, such as hexagonal cells and horizontal rolls, can often be seen from high flying aircraft or from a satellite perspective, if clouds are present. The photo in Figure 12 depicts characteristic cloud bands which indicate the presence of rolls in the atmosphere. The presence of horizontal roll vortices is marked by cloud streets which form in the regions of upward-moving air.

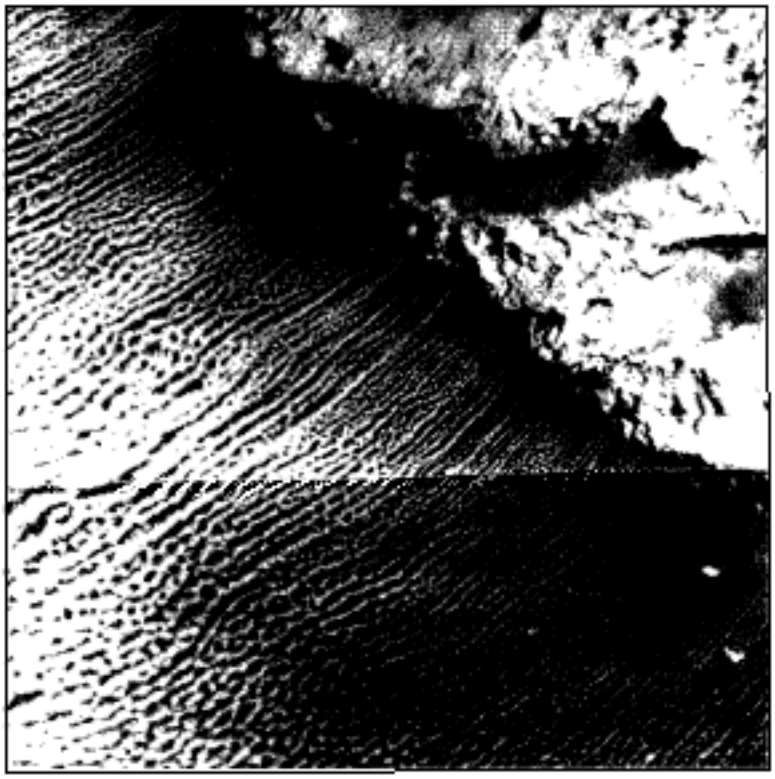

Figure 12. Cold air flowing off an ice pack over the Bering Sea. February 22 1983. (NOAA Satellite photo)

Studies of Brown (1980) that show the angle between the roll direction and the free stream vary from about 30^{o} in the stable case to about 5^{o} for the convective case. Kuettner (1959, 1971) found the following typical properties of rolls: length: 20 - 500 km, spacing: 2 - 8 km, height: 0.8 - 2 km, width/height ratio: 2 - 4 : 1. The structure of such rolls is very difficult to determine from tower measurements since their axes are parallel to the wind, their crosswind propagation velocity is small, and also because the spacing between rolls is several kilometers.

1.9 Small-Scale Circulations, Turbulence

Small-scale motions are characterized by a horizontal length scales from millimeters to a few kilometers. Consequently, they are considered local with respect to air pollutant sources. Small-scale motions can can be generated by temperature contrasts at the Earth's surface, wind shear, effects of the Earth's topography. They can also occur above the Earth's surface in statically stable flows or on a density discontinuity interfaces, when the destabilizing influence of the wind shear overcomes the stabilizing effect of the buoyancy force.

The last effect is called Kelvin-Helmholtz instability. If the static stability of the flow is not sufficient to dampen perturbations excited by the wind shear, they may amplify. Eventually the waves may break and dissipate into smaller scale complex and chaotic motion called turbulence. Turbulence is an essential part of the mechanism which disperses air pollutants and is crucial for the efficiency of many natural processes, such as the evaporation of water, dissipation of fog, and dispersion of plant seeds.

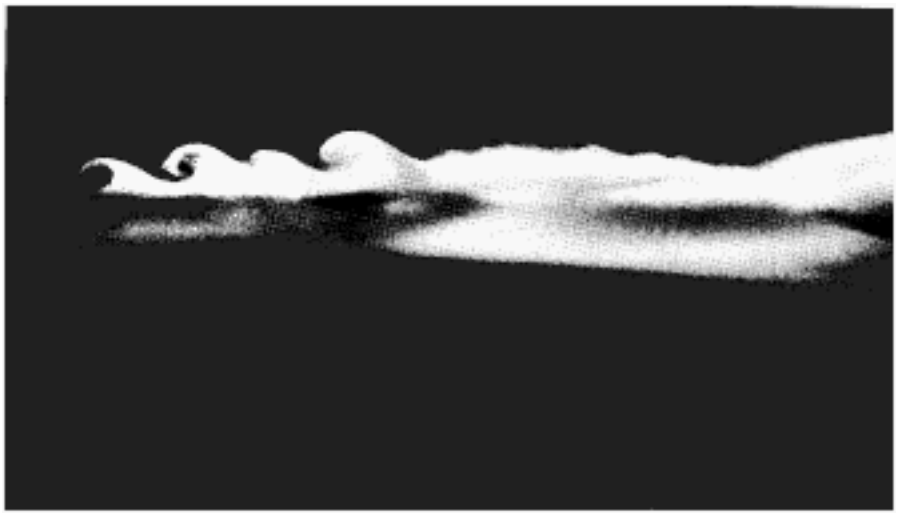

Figure 13. Kelvin-Helmholtz instability, revealed by the cloud patterns in the atmosphere (NCAR.NSF Photo Archive)

Kelvin-Helmholtz instabilities have been observed by radar [Gossard and Richter (1970), Gossard, et al. (1971), Gossard, et al. (1973), and Richter, et al. (1973)]. The internal waves, originated through Kelvin-Helmholtz instability, are typically several hundred meters in length. Their velocity of propagation was found to be about the same as the mean velocity of the layer in which they are embedded (Hooke, et al. 1973). With the passage of internal gravity waves, very thin shear layers of small-scale turbulence are observed moving up and down. Sometimes this type of instability is revealed by the cloud patterns on top of the boundary layer (Figure 13).

To further analyze small-scale motions let us assume that a horizontally homogeneous flow is affected by a small-scale disturbance characterized by length scale λ, velocity scale v_λ, and temperature scale θ_λ. The rate at which the kinetic energy of the motion is produced by the disturbance in the unit of time is:

$$R_{1\lambda} \sim v_\lambda^3 / \lambda \tag{11}$$

The kinetic energy of the disturbance is later employed as work against viscosity force:

$$R_{2\lambda} \sim \nu \, v_\lambda^2 / \lambda^2 \tag{12}$$

and also against the buoyancy force:

$$R_{3\lambda} \sim \beta \;\; \theta_\lambda \; v_\lambda \tag{13}$$

where $\beta = g/T$ is the buoyancy parameter. The disturbance persists only, if $R_{1\lambda} > R_{2\lambda} + R_{3\lambda}$. When the role of the buoyancy force is small then $R_{2\lambda} >> R_{3\lambda}$ *and* $R_{1\lambda} > R_{2\lambda}$, which is equivalent to:

$$\lambda v_\lambda / \nu = Re_\lambda > 1 \tag{14}$$

where Re_λ is the Reynolds number for the disturbance.

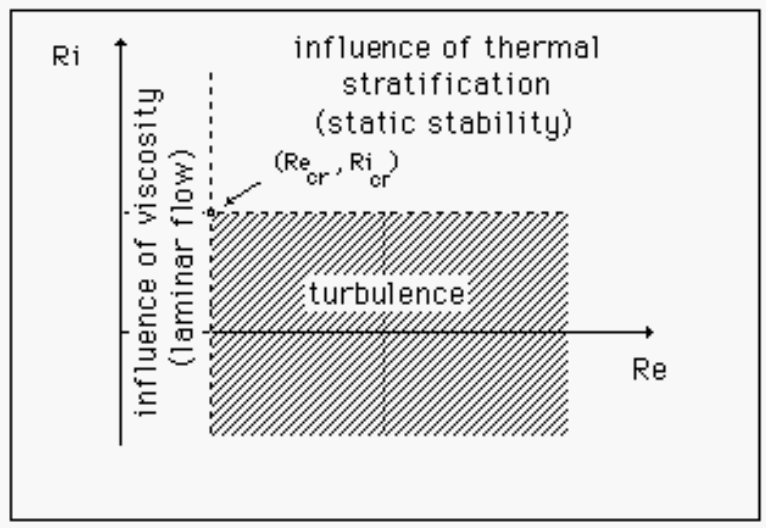

Figure 14. Regions of turbulent flows.

In contrast, if the role of the buoyancy force is large and $R3_\lambda >> R2_\lambda$ then $R3_\lambda < R1_\lambda$, which is equivalent to:

$$\beta \, \theta_\lambda \, \lambda / \varpi_\lambda^2 = Pt_\lambda < 1 \tag{15}$$

where Ri_λ is the Richardson number for the disturbance.

In conclusion, turbulence is maintained if the Reynolds number *Re* is larger or, more precisely, if it is greater than its critical value Re_{cr} and, similarly, if the Richardson number R_i is smaller than its critical value Ri_{cr}. This is illustrated in Figure 14.

To describe turbulence, it is convenient to adopt the approach of O.Reynolds (1842-1912) who in 1895 proposed decomposing any flow variable into a mean quantity (marked by overbars) and a fluctuation about the average (letters with primes). For example, for wind components and the potential temperature we have:

$$u_i = \overline{u}_i + u_i' \tag{16}$$

$$\Theta = \overline{\Theta} + \theta'$$

The averaging procedure can be defined in different ways, as time average, space average or ensemble average. In a conventional theoretical procedure the mean quantities are ensemble averages. It is assumed that atmospheric flows are members of an ensemble whose individual realizations obey the Navier-Stokes equations. Ensemble averages have the following properties:

$$u_i(t) = \lim_{N\to\infty} \frac{u_i(t;1) + \ldots u_i(t;N)}{N} \tag{17}$$

where $u_i(t; j)$ is the *j*-member of an ensemble of *i*-components of the wind velocity (i =1, 2, 3) and the overbar denotes the ensemble averaging operator. From (17) it follows that an ensemble average of a primed quantity is zero, and doubled averaging produces the same average. The average of the nonlinear term u_iu_j has the form:

$$\overline{u_i u_j} = \overline{u}_i \overline{u}_j + \overline{u_i' u_j'} \tag{18}$$

Thus, ensemble averaging of the product u_iu_j introduces additional terms $\overline{u_i' u_j'}$ called the Reynolds stress terms. Since i, j =1, 2, 3, there are 9 Reynolds terms. Because of symmetry, 3 terms are equal and only 6 terms are different.

Similarly, the average of the nonlinear temperature term has the form:

$$\overline{u_j \Theta} = \overline{u}_j \overline{\Theta} + \overline{u_j' \Theta'} \tag{19}$$

The ensemble averaging of the products $u_j\Theta$ introduces 3 additional terms.

In order to explain the meaning of the additional terms which appear in (18)-(19), consider two horizontal layers of air flow with slightly different horizontal velocities and temperatures. The random vertical intrusions of some slower

parcels of air into the faster stream tend to slow down the faster stream. The intrusion of faster parcels into the slower stream tend to speed up the slower stream. Similarly intrusions of cooler parcels of air will cool while intrusions of warmer parcels will warm the stream. Therefore, the wandering of individual parcels introduces the vertical momentum (stress) and the heat flux in the turbulent flow. The resulting horizontal turbulent stress vector is usually denoted as $\boldsymbol{\tau} = \left(-\rho\overline{u'w'}, -\rho\overline{u'w'}\right)$ where ρ is the air density. The vertical heat flux can be expressed as $H = c_p\,\rho\overline{w'\Theta'}$, where conventional meteorological notation was applied: $u_1 = u$, $u_2 = v$, $u_3 = w$, and c_p is the specific heat of dry air.

2 Boundary-Layer Meteorology

2.1 General Description

The planetary boundary layer (PBL) is the lowest portion of the atmosphere, about 1 - 2 km deep, which intensively exchanges heat as well as mass (water, gases) with the Earth's surface. Although the PBL contains only about 2% of the total kinetic energy of the atmosphere, it contributes as much as 25% to its total generation and 35% to its total dissipation. The atmospheric boundary layer is of great practical and scientific importance. Essentially, all human and biological activities take place in this layer. Practically all air pollutants from natural and anthropogenic sources are emitted within the PBL.

Flow in the boundary layer is controlled by the diurnal cycle of the surface energy budget. The energy balance at the surface is expressed as $R_n + G + H + E = 0$, where R_n is the flux of net radiation (global solar radiation received by the surface plus atmospheric radiation minus terrestrial radiation), G is the vertical heat flux into the soil, H and E are the sensible (conduction) and latent (resulting from water phase changes) heat fluxes to the atmosphere. The diurnal changes of the energy balance are shown in Figure 15.

In Figure 15, a quantity has a positive value, when energy is transferred away from the interface, and a negative value in the case of transfer towards the interface. Net radiation flux R_n is negative (down) during the day, reaching minimum values at local solar noon. At night, R_n is positive, illustrating the loss of energy by terrestrial radiation. R_n is zero just before sunset, and just after sunrise. At night, the term E can become negative, if dew forms.

During the day, energy gained at the surface is transferred to the atmosphere, to the soil, and also is used in the evaporation processes. This transfer of heat, from the ground surface to the air directly above it,can generate vertical motions, called convection. Convection redistributes heat throughout the atmospheric boundary layer. The influence of the surface sensible heat flux decreases with height. As a result, the diurnal temperature amplitude also decreases with height.

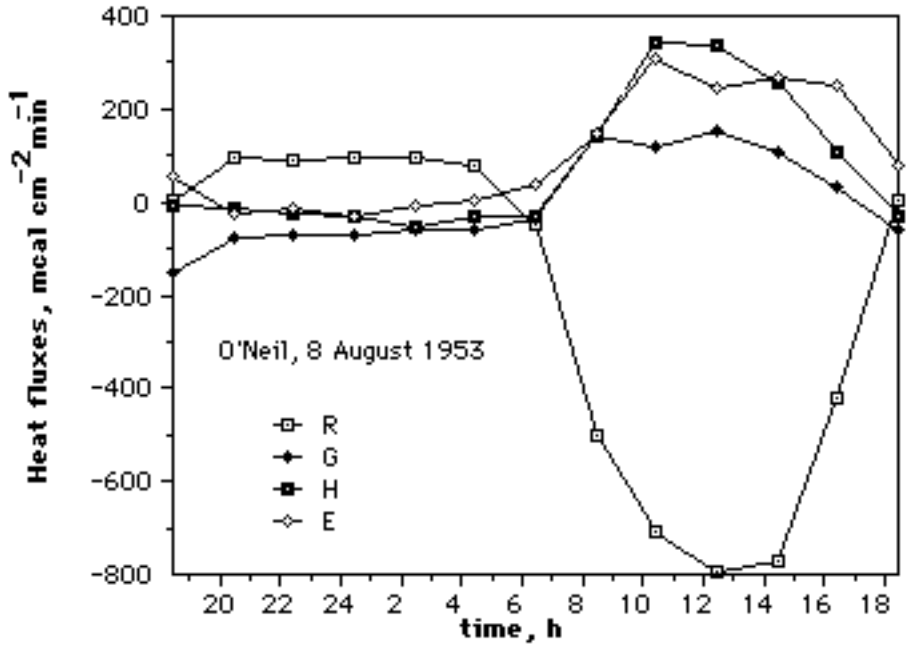

Figure 15. Diurnal distribution of heat fluxes at the Earth's surface, during the 1953 O'Neil experiment. *R* is the flux of net radiation on the surface, *G* is the heat flux to the ground, *H* is the sensible heat flux and *E* is the latent heat flux from the surface to the atmosphere (after Sorbjan, 1989).

It is generally assumed that over a flat and homogeneous surface, the planetary boundary layer is horizontally homogeneous, but organized vertically into several layers (Figure 16). Within a few millimeters of the surface, there is a viscous sublayer, where the flow is mostly laminar. Above this layer, there is a surface layer, 1-100 m deep, where the turbulent fluxes of momentum, heat, and moisture are approximately constant with height (i.e., they change in magnitude no more than 10% from their surface values).

The wind direction in the surface layer is approximately constant with height. In the first few meters of the surface layer the wind velocity, humidity, and temperature are nearly logarithmic in neutral, and also in stable and convective conditions. Above the logarithmic sublayer the profiles of various meteorological parameters differ depending on thermal stratification. The portion of the boundary layer beyond the surface layer is called the outer layer.

In day-time conditions the potential temperature, humidity and wind velocity in the outer layer are approximately constant with height, and the layer is often called the "mixed layer". At night, the temperature inversion is usually formed near the surface. In the upper portion of the outer layer, called the residual layer, the potential temperature remains constant with height. At the level of few hundred meters above the surface, the wind velocity reaches a maximum, and exceeds the value of the geostrophic wind. This maximum is often called the "low-level nocturnal jet".

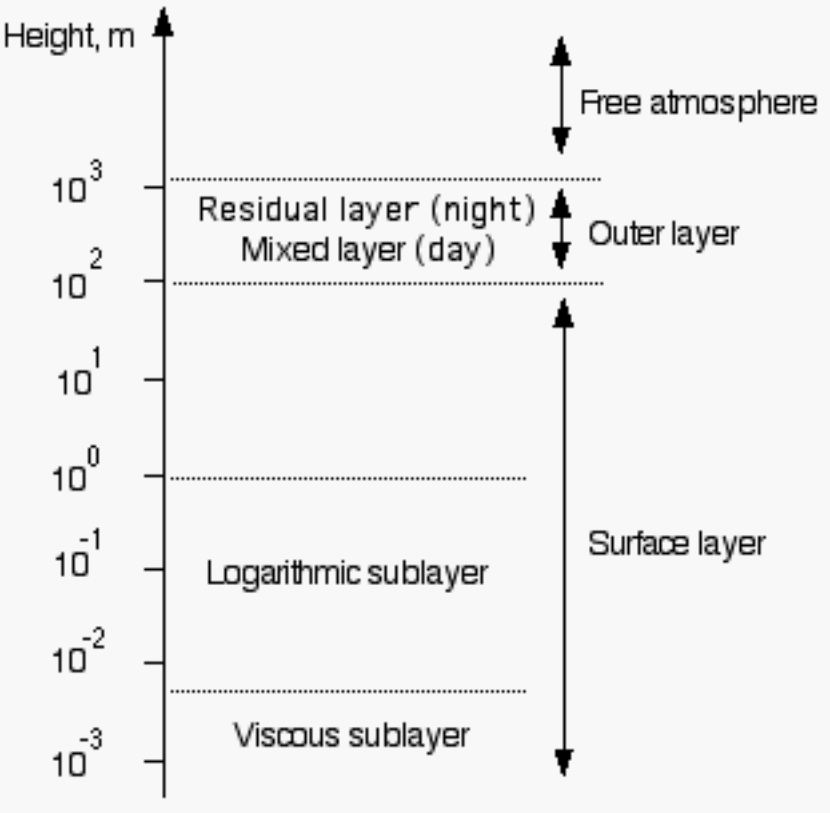

Figure 16. A schematic structure of the planetary boundary layer.

The diurnal changes of temperature are accompanied by changes of wind velocity and wind direction. Above the surface layer the winds are observed to reach maximum speeds at night and minimum speeds during the day. But near the surface, the opposite behavior of wind velocity is observed. The surface wind speed increases after sunrise, peaks in the early afternoon and decreases near sunset. Above the surface layer, the diurnal wave is nearly 12 hours out of phase.

Friction causes the wind velocity in the boundary layer to cease to zero at the surface. The wind direction varies with height because of the influence of the Coriolis force. The latter fact was first discovered in the ocean by F.Nansen (1861-1930), and later explained by V.V.Ekman (1874-1954) in 1905. By examining data from the 1893-1896 Norwegian North Polar Expedition, Nansen noted that sea ice did not drift in the direction of the wind, but at an angle of about 40^o to the right of the wind direction (Figure 17). Based on this observation Ekman concluded that each layer of the sea was set in motion by the layer just above it, and successively more deflected by the balance of the Coriolis and friction forces. In honor of his work, the spiraling of the currents in the ocean is named the Ekman spiral.

It was realized later that the Ekman spiral can be observed not only in the ocean but also in the atmospheric boundary layer, where winds in average spiral with height from about 5^o (during the daytime) to about 50^o at night, clockwise in the

northern hemisphere, but counter-clockwise on the southern hemisphere. The spiraling effect in the atmosphere is caused by the balance of the Coriolis, pressure gradient, and friction forces, and strongly depends on thermal stability. Note that thermal advection of cold or warm (baroclinicity) air can strongly modify this picture.

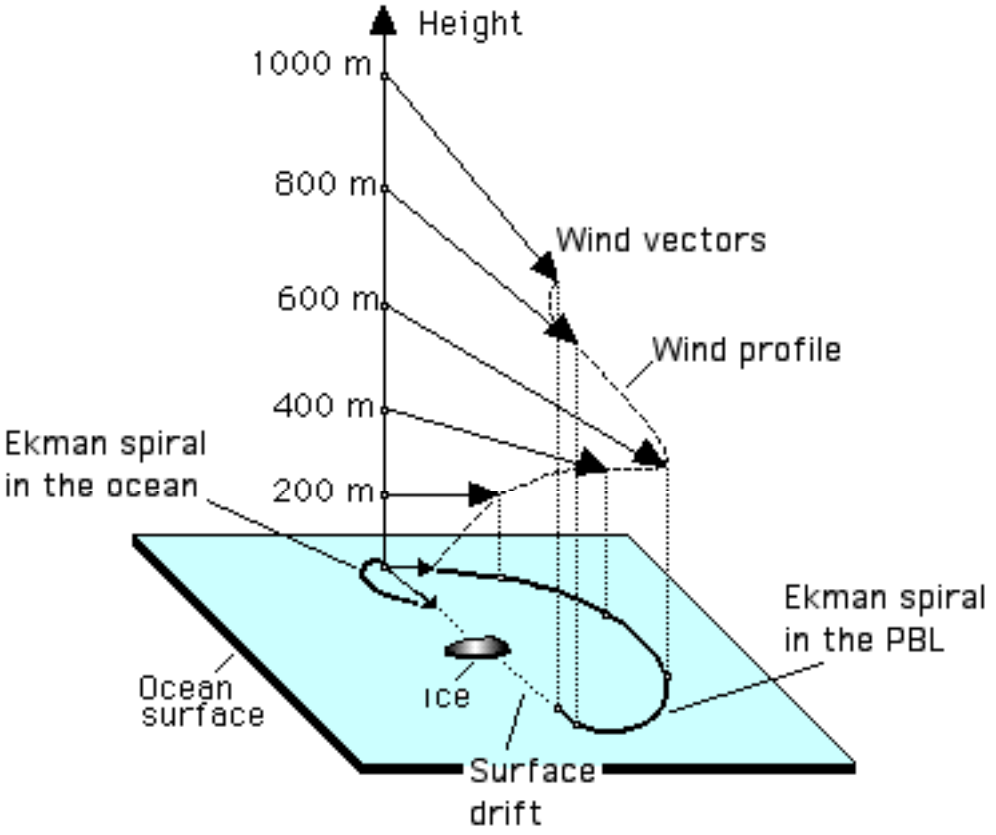

Figure 17. The Ekman spirals in the atmosphere and in the ocean.

During the last several decades, the structure of the atmospheric boundary layer has been intensively studied, not only because of the striking beauty of its coherent structures (e.g., Agee, 1987), but mostly because understanding its flows and clouds is essential in environmental studies, numerical weather prediction, and climate analyses. As a result, since the 1950s, the fundamental knowledge of boundary layer turbulence has been achieved as a result of extensive experimental effort, and also due to numerical modeling. Especially, large-eddy simulations (LES) contributed to our present knowledge of turbulence and diffusion in the ABL (e.g., Deardorff (e.g., 1970, 1972, 1974 a, b, 1976; Mason, 1989; Moeng, 1984, 1998, Moeng and Sullivan, 1994; Nieuwstadt et al., 1992, Schem and Lipps, 1976; Schmidt, H., and U. Schumann, 1989, Sommeria, G., 1976, Sorbjan, 1996 a, b, 1997).

2.2 Viscous and Logarithmic Sublayers

A simple analytical formulation of idealized conditions in the atmospheric boundary layer can be obtained based on similarity and dimensional analysis (Buckingham, 1914). During the last four decades the elegant similarity framework has allowed classification of knowledge on atmospheric turbulence obtained through extensive experimental effort.

The idea of similarity lies in dimensional analysis. The method is based on the assumption that some physical quantities which are necessary and sufficient to describe a certain physical phenomenon are dimensionally dependent on others. One can then form dimensionless groups of these variables which are independent of the system of units chosen: $\pi_o = f(\pi_1, \pi_2, ..., \pi_{n-r})$, where n is the number of physically relevant variables, such as velocity, density, stress, and r is the number of independent physical units, such as length, time, mass, and the πi are the nondimensional products. A group of variables which is applied in order to nondimensionalize another variable is often called a scale (e.g., Sorbjan, 1989).

To describe the mean flow in the viscous layer we will seek an expression for the mean wind shear using the π-theorem. We first assume that $dU/dz = f(u_*, \nu, z)$, where $u_* = (\tau_o/\rho)^{1/2}$ is the friction velocity -- representing the surface stress, ν, is the molecular viscosity and z is the height. Based on this assumption, the following two nondimensional groups may be formed: $\pi_o = z/u_* \, dU/dz$, and $\pi_1 = zu_*/\nu$. The first group is the nondimensional wind shear, and the second one may be recognized as the local Reynolds number. In the viscous sublayer, both parameters can be assumed to be of the same order of magnitude, i.e., $z/u_* dU/dz \sim zu_*/\nu$. We may integrate this expression to determine:

$$U \sim u_*^2 z / \nu \tag{20}$$

for the velocity in the viscous sublayer.

Above the viscous layer, the two parameters π_o and π_1 are not of the same order of magnitude. For z = 10 m, u_* = 0.1 m/s, and $\nu = 10^{-5}$ m^2/s, one can easily verify that the wind shear is 0(1), and the Reynolds number is Re ~ $u_* z/\nu \sim 10^5$. This difference in magnitude reflects the empirical fact that the viscous stress is negligible compared to the turbulent stress in the surface layer. Thus, for a similarity solution $\pi_o = F(\pi_1)$ to exist in the surface layer (where π_1 is large), F must be asymptotically constant when π_1 is large i.e., for $\pi_1 \to \infty$, $F(\pi_1) \to const$. This yields: $z/u_* \, dU/dz = const = \kappa^{-1}$, where κ is the von Karman constant, empirically estimated to be 0.4. The obtained result may be integrated to yield the logarithmic profile:

$$U(z) = \frac{u_*}{\kappa} \ln\left(\frac{z}{z_o}\right) \tag{21}$$

where the roughness parameter z_o is an integration constant that represents the aerodynamic roughness of the underlying surface. Note that at $z = z_o$, the wind velocity vanishes.

The similarity approach may also be employed to characterize the roughness parameter, z_o, of a homogeneous surface with physical roughness elements of characteristic height, h_o. Applying the π-theorem we obtain: $z_o/h_o = F(u_* h_o/\nu)$, where the product $u_* h_o/\nu$ is the roughness Reynolds number Re_r. The thickness of the viscous sublayer is characterized by the parameter $\delta \sim \nu/u_*$.

When the $Re_r << 1$, then $h_o << \delta$, and the roughness elements are completely submerged in the viscous sublayer. In this hydrodynamically smooth case, we must drop h_o from the list of the governing parameters. Consequently, $z_o/h_o \sim Re_r^{-1}$ or $z_o \sim \nu/u_*$. If $Re_r >> 1$, then $h_o >> \delta$, and the roughness elements protrude beyond the viscous sublayer, i.e., the flow is called hydrodynamically rough. We may claim that for $Re_r \to \infty$, $F(Re_r)$ becomes a constant. The conclusion is $z_o \sim h_o$.

2.3 Surface Layer

Turbulence in the thermally stratified surface layer can be elegantly characterized in terms of the surface layer similarity theory. The theory was formulated about five decades ago by A.S.Monin and A.M.Obukhov (1954). Since then a simple and effective framework of this approach has found many practical applications in experimental analysis of surface layer turbulence, as well as in the parametrization of mass and energy exchange across the Earth's surface.

According to the Monin and Obukhov (M-O) theory, similarity scales in the surface layer can be formulated based on constant values of the kinematic turbulent fluxes $H_o = \overline{w'\theta'}$, $Q_o = \overline{w'q'}$, *and* $\tau_o / \rho = \overline{w'u'}$:

$$u_*^2 = \tau_o/\rho, \quad T_* = -H_o/u_*, \quad q_* = -Q_o/u_*, \quad L = u_*^2/(\beta \kappa T_*) \tag{22}$$

where u_*, T_*, q_*, L are the velocity, temperature, humidity (or other scalars, such as ozone or carbon dioxide concentration), and height scales respecively, $\beta = g/T_o$ is the buoyancy parameter, and L is called the Monin-0bukhov length. The sign convention is chosen so that L is negative in unstable and positive in stable stratification. Note that the potential temperature flux H_o in the definition of T_* and L should be replaced by the virtual potential temperature flux H_{ov} when moisture stratification is included. The virtual potential temperature flux is defined as $H_{ov} = H_o + 0.61\ T\ Q_o$, where Q_o is the surface humidity flux. The virtual temperature Θ_v is defined as $\Theta_v = \Theta\ (1 + 0.61\ q)$, where q is the specific humidity.

The Monin-0bukhov length L is roughly the height at which the shear production of turbulent kinetic energy ($= u_*^3/L$) is equal to the buoyant production ($= \beta H_o$). In

the stable boundary layer $H_o < 0$, $T_* > 0$ and $L > 0$. In the unstable boundary layer $H_o > 0$, $T_* < 0$ and $L < 0$. In this case, the turbulent energy production is mainly mechanical (produced by shear) for $z < -L$ (closer to the surface) and buoyant (produced by the heat flux) when $z > -L$.

The similarity theory predicts that any turbulent characteristics of the flow, non-dimensionalized with surface layer scales, will be a universal function of the stability parameter $\zeta = z/L$, e.g.,

$$\frac{\overline{w'^2}}{u_*^2} = \Psi_w(z/L), \qquad \frac{\overline{\theta'^2}}{T_*^2} = \Psi_\theta(z/L), \qquad \frac{\overline{q'^2}}{q_*^2} = \Psi_q(z/L),$$

$$\frac{L}{u_*}\frac{dU}{dz} = \Psi_m(z/L), \qquad \frac{L}{T_*}\frac{d\Theta}{dz} = \Psi_h(z/L), \qquad \frac{L}{q_*}\frac{dq}{dz} = \Psi_q(z/L) \tag{23}$$

where U, Θ, and q are the mean wind velocity, potential temperature and specific humidity. Usually, the nondimensional gradients are divided by $\zeta = z/L$ and substituted by new similarity functions ϕ, defined as: $\phi_m = \zeta \psi_m$, $\phi_h = \zeta \psi_h$, $\phi_q = \zeta \psi_q$. Consequently:

$$\frac{z}{u_*}\frac{dU}{dz} = \Phi_m(z/L), \qquad \frac{z}{T_*}\frac{d\Theta}{dz} = \Phi_h(z/L), \qquad \frac{z}{q_*}\frac{dq}{dz} = \Phi_q(z/L) \tag{24}$$

where ϕ_m , ϕ_h and ϕ_q are new similarity functions.

Monin and Obukhov pointed out that the limiting forms of the similarity functions can be determined for three extreme stratification regimes -- neutral, very stable, and very unstable (free-convection).

In neutral stratification, the heat flux is zero, and $z/L = 0$. Thus, all similarity functions ψ must be constant. Consequently ϕ_m, ϕ_h. $\phi_q \sim \zeta^{-1}$ (and L cancels). This leads directly to logarithmic profiles for wind velocity, temperature and humidity (or other passive scalar). Note that logarithmic profiles are obtained for $0 < |z/L| << 1$ (neutral stratification), and also for $0 < z << |L|$ (any stratification very close to the surface).

In the very stable layer, when $z/L \to \infty$, z is no longer a governing variable. Physically, this means that the turbulence is local and suppressed by stratification effects. In this case, $\phi_m \sim \zeta$, $\phi_h \sim \zeta$ and $\phi_q \sim \zeta$, so "z" crosses out on both sides of (24). This leads to linear velocity, temperature, and humidity profiles.

In the free-convection case ($z/L \to \infty$), the mean wind is negligible, so $u_* \to 0$ (no surface stress), As a result, u_* must be dropped from the list of governing

variables. This leads to a new set of scales: $u_f = (\beta z H_o)^{1/3}$ for velocity, $T_f = H_o/u_f$ for temperature, $q_f = Q_o /u_f$ for humidity (Wyngaard et al., 1971). Note that there is no specific height scale in this case. If we form new nondimensional quantities using these scales, we expect them to be constant, because there is no dimensionless height parameter in this case, which would be equivalent to z/L.

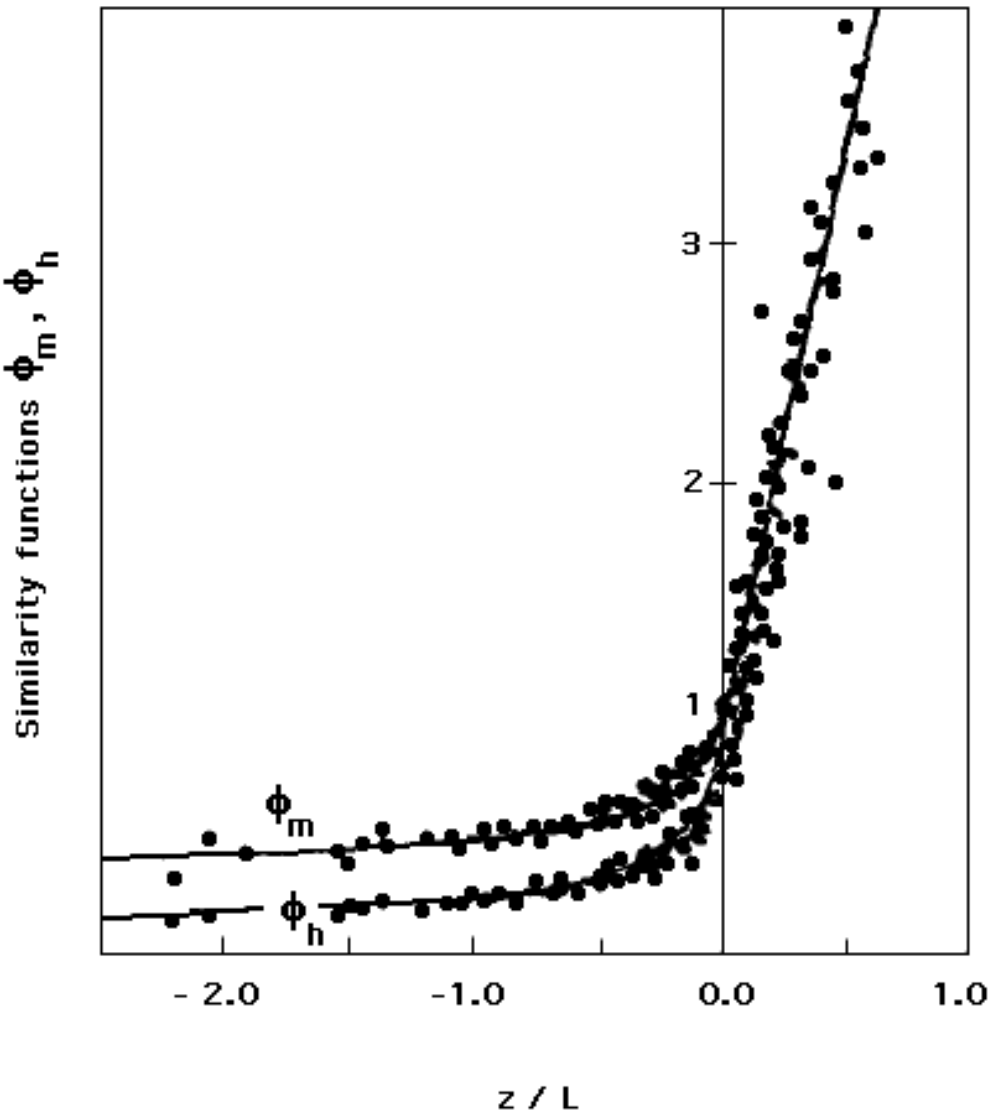

Figure 18. M-O similarity function for wind velocity ψ_m, and temperature ψ_h from the Kansas experiment. The data have been fit with formulas $\phi_m = (1 - 15\,\zeta)^{-1/4}$ and $\phi_h = 0.74\,(1 - 9\,\zeta)^{-1/2}$ for $\zeta < 0$, and $\phi_m = (1 + 4.7\,\zeta)$ and $\phi_h = 0.74 + 4.7\zeta$ for $\zeta > 0$ (after Businger et al, 1971).

The direct application of the free-convection scales yields to a prediction for the potential temperature, obtained earlier by Monin and Obukhov: $z/T_f\, d\Theta/dz = const$. Taking into consideration that $T_*/T_f = \kappa^{-1/3}\,(-z/L)^{1/3}$, this implies that the dimensionless temperature gradient ϕ_h is proportional to $(-z/L)^{-4/3}$. Consequently,

the mean temperature varies with height as $z^{-1/3}$. In forced convection (convection with wind shear), we could assume that the ratio of momentum and heat fluxes can be evaluated as: $(\tau_o/\rho) / H_o = u_*^2 / (u_* T_*) = (K_m\, dU/dz) / (K_h\, d\Theta/dz)$, where K_m and K_h are the eddy viscosity and diffusivity. Assuming that in this case, the Prandtl number $Pr = K_m / K_h = constant$, we will obtain $\phi_m \sim \phi_h$. This indicates that the mean wind in forced convection should also be proportional to $z^{-1/3}$.

Validity of the Monin and Obukhov surface layer similarity theory has been extensively tested during the last few decades. The measurements of Zilitinkevich and Chalikov (1968) confirmed the convective prediction $\zeta^{-1/3}$ for ψ_m and ψ_h, where $\zeta = z/L$. On the other hand, in the famous "Kansas" field experiment, e.g., Businger et al. (1971), the dependence of the nondimensional temperature gradient and shear profiles (Figure 18**)** were found to be: $\psi_m \sim \zeta^{-1/4}$ and $\psi_h \sim \zeta^{-1/2}$ for $\zeta > -2$. A later experiment using the BAO tower in Colorado (Kaimal et al., 1982) verified the free-convection limit predictions for standard deviations (Figure 19).

In the stable surface layer, observations confirm similarity predictions, however, the scatter increases as ζ increases. Measurements in this case are very difficult to make due to low levels of turbulence intensity. The increased scatter is most likely due to the increased importance of gravity wave effects.

At this point, words of caution should be expressed that making automatic assumptions regarding dimensional analysis can lead to conclusions that do not reflect reality (e.g., Sorbjan, 1993). For example, refer to Figure 20. In Figure 20a, dimensionless vertical velocity standard deviation follows the M-O theory prediction $\sigma_w/u_* \sim (-\zeta)^{1/3}$ in the convective limit. A similar prediction may be made for the horizontal velocity standard deviations σ_u or σ_v, and Figure 20b appears at first glance to confirm this prediction. However, on closer examination, if the data are grouped either by constant L value, or by constant height. z, (Figure 20 c and d), we see that the data are independent of z. Thus, σ_u is independent of ζ and does not follow the M-0 similarity theory. It was later determined that σ_u depends on the non-dimensional parameter $-z_i / L$ because of the influence of large (PBL-scale) eddies on the surface layer turbulence statistics (Panofsky et al., 1977).

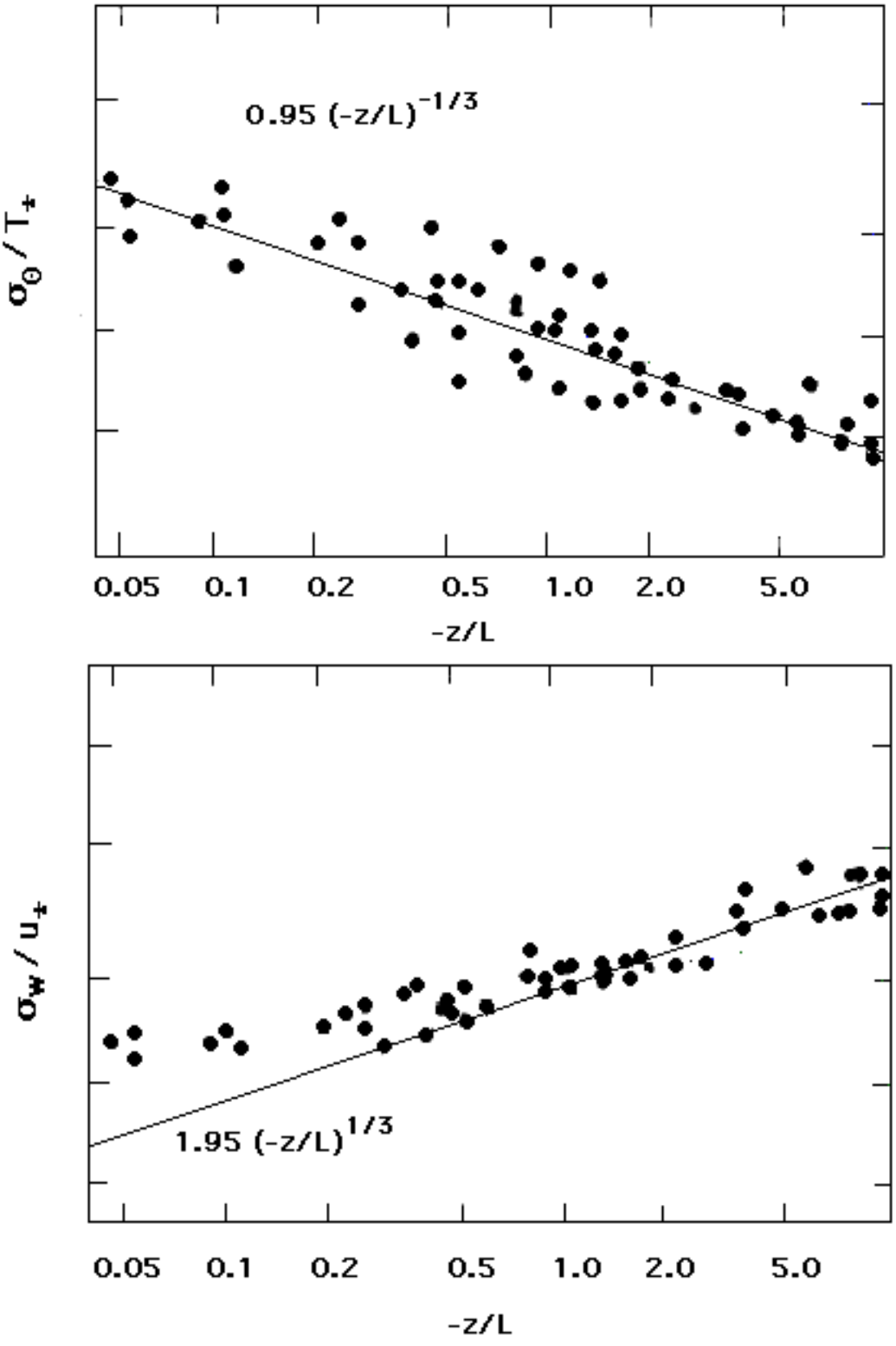

Figure 19. Non-dimensional profiles of the standard deviations σ for (a) temperature, and (b) vertical velocity, as functions of z/L in unstable stratification (after Kaimal et al., 1982).

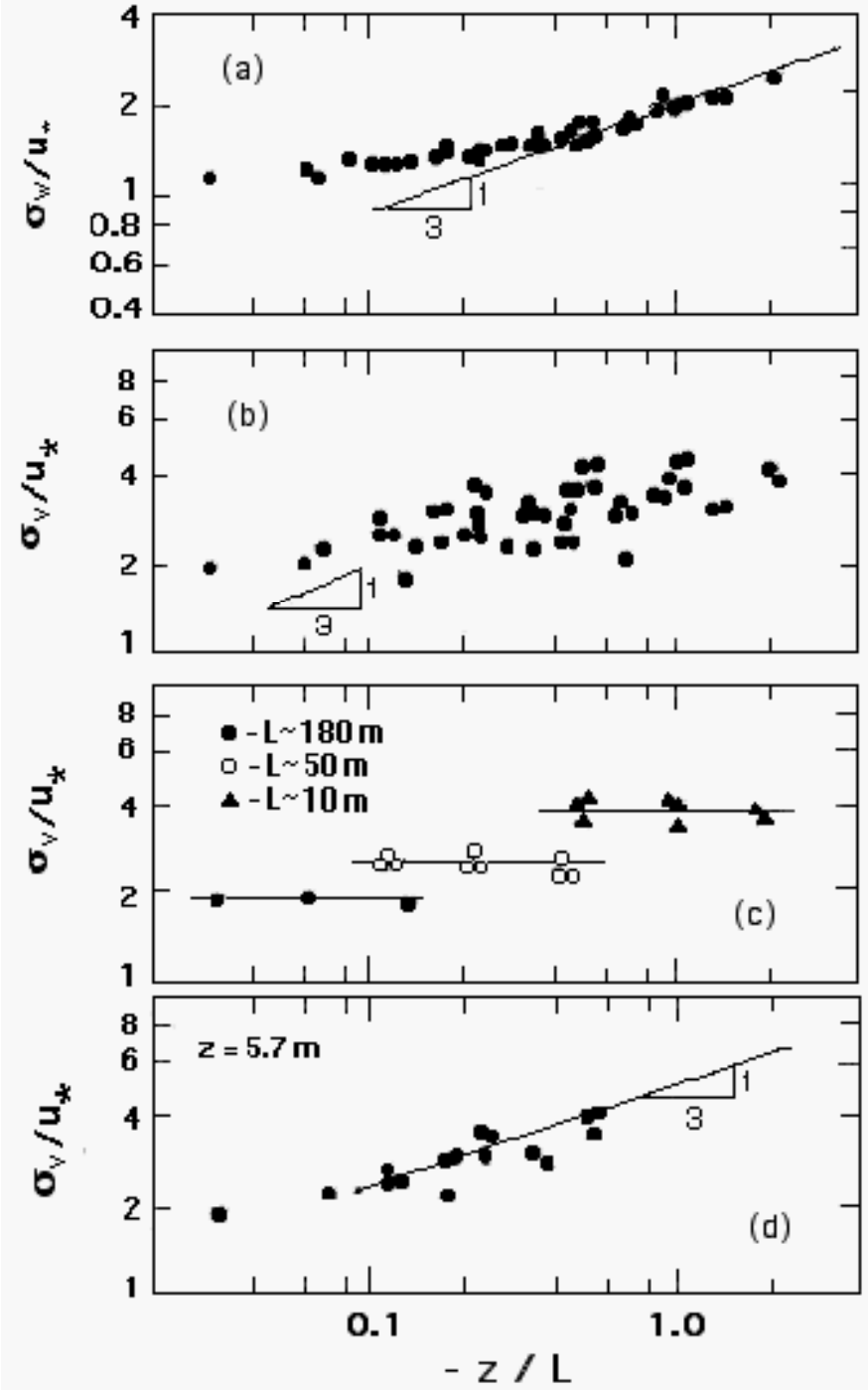

Fig. 20. (a) The standard deviation of the vertical velocity in unstable stratification. Note that the data follow the "1/3" law as the stratification becomes more unstable. (b) The standard deviation of the horizontal velocity in unstable stratification. Note that the data appear to follow the "1/3" law as well, although there is more scatter than for the vertical velocity. (c) The same data as in (b) except only those data with L=-180, -50, and -10 m are plotted. (d) The same data as in (b) except only those data for z=5.7 m are plotted (after Wyngaard, 1988).

2.4 Stable Outer Layer

The success of the Monin-Obukhov theory in the surface layer has raised natural questions, such as whether the upper portion of the boundary layer also has a self-similar structure, and whether this structure can be expressed in terms of an equally simple and elegant approach. The positive answer to these questions in the case of the moderately stable boundary layer was found by Nieuwstadt (1984), who introduced the local (height dependent) similarity scales. Based on these local scales, the M-O similarity functions for various statistical moments, spectra, and cospectra, could be simply extended for the entire stably stratified boundary layer (Sorbjan, 1986, Sorbjan, 1988 a, b, Sorbjan, 1989, Sorbjan, 1995).

Let us introduce the following height-dependent, local similarity scales for velocity. temperature, humidity, and length:

$$
\begin{aligned}
U*(z) &= \left[\overline{u'w'}^2 + \overline{u'w'}^2\right]^{1/4} \\
\Xi*(z) &= -\frac{\overline{w'\theta'}(z)}{U*(z)} \\
Q*(z) &= -\frac{\overline{w'q'}(z)}{U*(z)} \\
\Lambda*(z) &= -\frac{U_*^2(z)}{\kappa\beta\Xi*(z)}
\end{aligned}
\tag{25}
$$

Note that the fluxes in the above definitions are functions of height. In the surface layer, where all fluxes are approximately constant, the above scales coincide with the surface layer scales u_*, T_*, q_*, and L, which were previously introduced.

One can argue that in stable stratification, turbulence is suppressed by buoyancy, and its characteristics should be local. Consequently, similarity functions obtained by non-dimensionalization with the local scales (12) should be constant (Sorbjan, 1986), e.g.:

$$
\frac{\overline{w'^2}}{U_*^2} = const, \qquad \frac{\overline{\theta'^2}}{\Xi_*^2} = const, \qquad \frac{\overline{q'^2}}{Q_*^2} = const, \tag{26}
$$

$$
\frac{\Lambda*}{U*}\frac{dW}{dz} = const, \qquad \frac{\Lambda*}{\Xi*}\frac{d\Theta}{dz} = const, \qquad \frac{\Lambda*}{Q*}\frac{dq}{dz} = const
$$

where W is the wind vector modulus. It can be noted that the above local similarity predictions coincide with the M-O functions, defined in the previous

section. For example, the surface layer prediction for the wind velocity is: $dU/dz = u_*/\kappa z\ (1 + 4.7\ z/L)$ (Businger et al., 1971). Its "outer layer" analog can be written as $dW/dz = U_*/\kappa z\ (1 + 4.7\ z/\Lambda)$. Note that the local similarity theory does not predict how the wind direction varies with height.

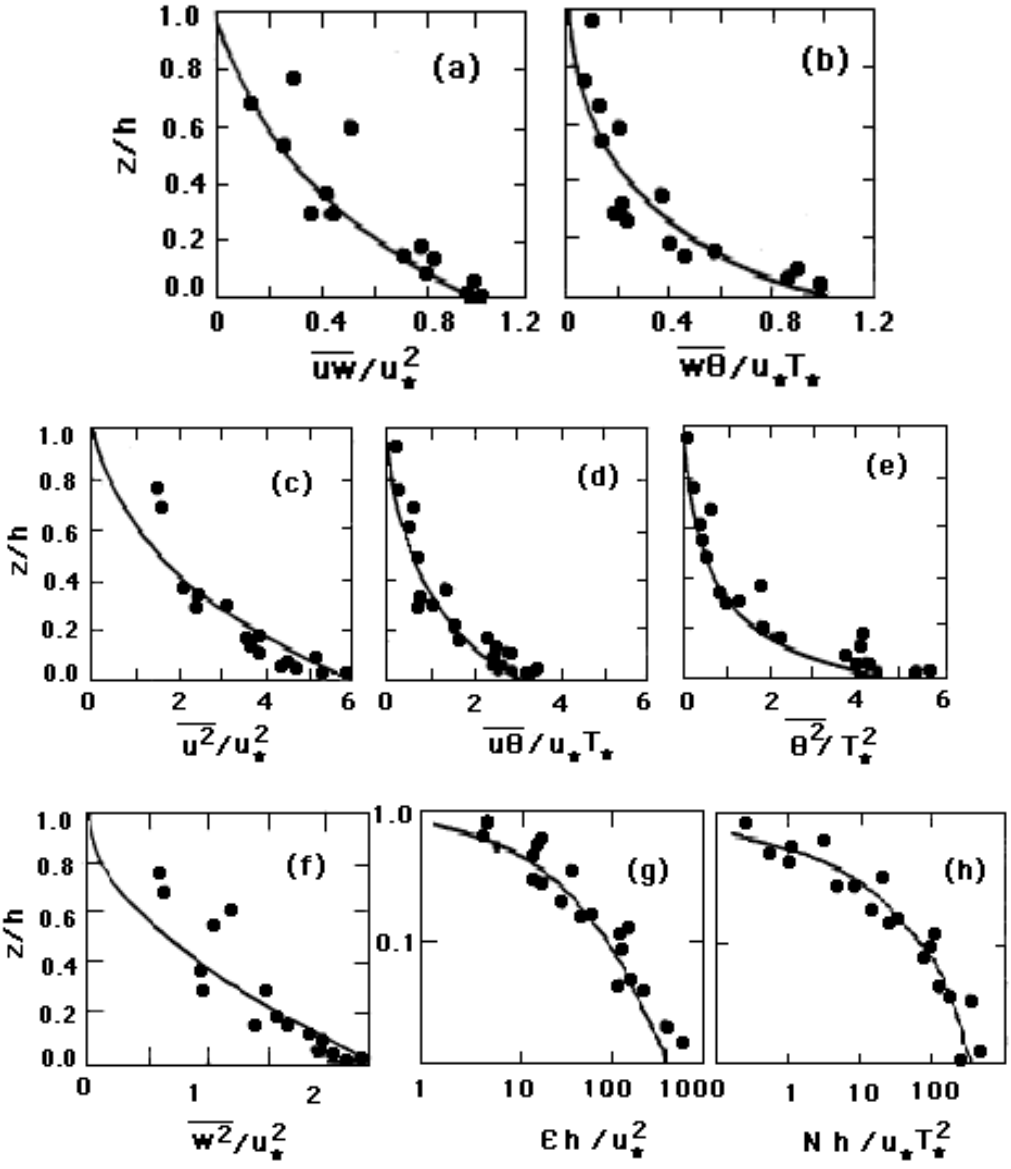

Figure 21. Comparison of the local similarity predictions (curves) in the stable boundary layer with the 1973-Minnesota data (dots):
a. the momentum flux, b. the vertical heat flux, c. the horizontal velocity variance, d. the horizontal heat flux, e. the temperature variance, f. the vertical velocity variance, g. the dissipation of the turbulent kinetic energy, h. the distruction of the temperature variance. In the figure, the presented moments are scaled by the friction velocity u_*, temperature scale T_* and depth of the stable boundary layer h.

We may assume now that the distributions of stress and heat flux with height can be expressed as follows:

$$U_*^2(z) = u_*^2 \, (1 - z/h)^{\alpha_1} \tag{27}$$

$$H(z) = H_o \, (1 - z/h)^{\alpha_2}$$

where h is the depth of the stable layer, defined as the level of the nocturnal jet, u_* is the friction velocity, H_o, is the surface value of the heat flux, and α_1 , α_2 are parameters.

The values of α_1 and α_2 must be found empirically, and are case dependent. Once they are determined, all turbulent statistics of the flow may be predicted. For example, based on (13) and (16), we can obtain the following prediction for the temperature lapse rate:

$$L / T_* \, d\Theta/dz = C \, (1 - z/h \,)^{2(\alpha_2 - \alpha_i)} \tag{28}$$

where C is an empirical constant, which can be evaluated from surface layer measurements. To avoid singularity at $z = h$, we must require, $\alpha_1 \leq \alpha_2$.

To illustrate how local similarity predictions agree with atmospheric observations, we will present results from the 1973 Minnesota experiments. Based on data collected during the 1973 Minnesota experiment (Figures 21a and 21b), we found that $\alpha_1 = 2$ and $\alpha_2 = 3$ (Sorbjan, 1986). From this, the local scales (25) and local predictions (26) were evaluated and are shown in Figures 21c - 21h.

2.5 Convective Outer Layer

After sunrise on a clear day, the Earth's surface becomes warmer than the air above it. The sensible heat is transferred from the ground to the air, causing intense convective mixing within the boundary layer. Depending on the time which has elapsed since the sunrise, the convective boundaryr layer over land usually exists in one of the following four regimes: morning convection, morning free-encroachment, early afternoon convection, and late afternoon decaying convection.

During the early morning convection, the surface heat flux increases with time (see Figure 16). Convective thermals erode the temperature inversion and the "mixed layer" is formed (Figure 22). Free-encroachment takes place when the mixed layer starts growing into a residual of the well-mixed layer from the previous day. During early afternoon convection, the surface heat flux is nearly constant with time. In the late afternoon, the surface heat flux begins to weaken and convection decays.

2.5.1 Morning Convection

Despite of a fast growth in time of the surface heat flux and the height of the mixed layer, early morning convection is usually in a quasi-steady state. As a result, the heat flux is linear with height. The value of the heat flux at the top of the mixed layer is negative and approximately equal to 20% of the surface value. In the developing mixed layer, potential temperature, specific humidity, wind velocity, and wind direction are nearly uniform with height (not in time).

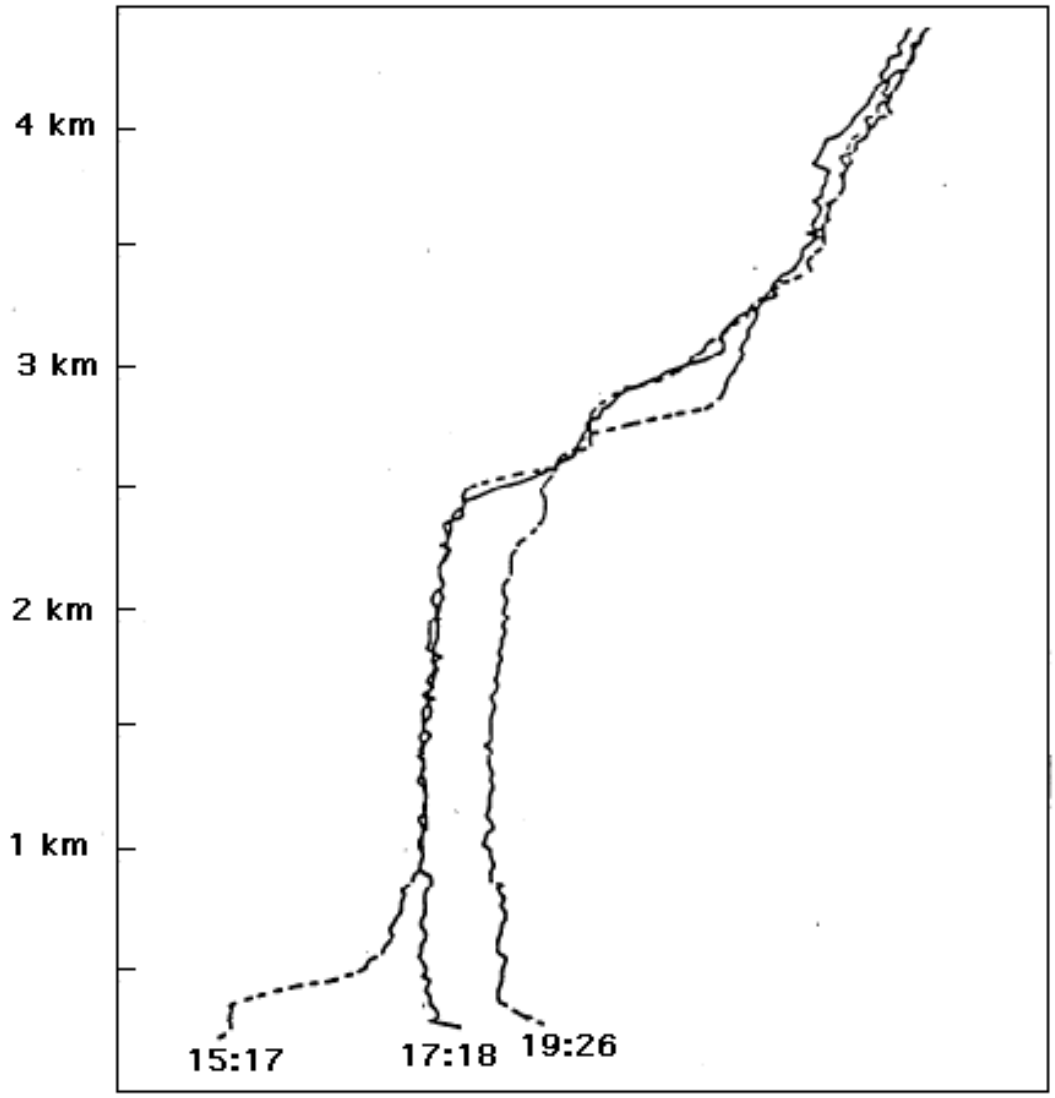

Figure 22. Sounding of the potential temperature measured on 10.07.1994 during Boreas experiment at 15:17, 17:18 and 19:26 GMT (9:17, 11:18, 12:16 LT). In the figure, the free-encroachment occurs around 17 GMT (11 LT) (after McPherson and Betts, 1995).

When an elevated residual mixed layer, left over from the previous day, becomes part of the newly growing mixed layer, free encroachment takes place (Figure 23). It lasts typically from a few minutes to about an hour. During this regime, updrafts penetrate the residual layer, nevertheless, the entrained air does not differ thermally from the air in the mixed layer. This causes the heat flux at the top of the mixed layer to vanish (Sorbjan, 1996b). Convection during encroachment is not in a steady-state. The heat flux is non-linear due to the intense growth of the mixed layer into the neutrally stratified layer, with a zero gradient Γ. This fact explains the role of the temperature gradient Γ, as the factor controlling a growth of the mixed layer. When Γ is near zero, a non-steady (growing) mixed layer is developed. When Γ is large enough, the resulting mixed layer is in a quasi-steady state with a linear heat flux profile.

2.5.2 Early Afternoon Convection

Early afternoon convection is in a quasi-steady state, due to the fact that the surface heat flux is nearly constant with time (Figure 15). In this state, the time rate changes of turbulent quantities can be ignored as small with respect to the dominant production and dissipation terms. In the mixed layer, meteorological parameters (potential temperature, humidity, wind) are nearly uniform with height. At the same time, profiles of the heat flux, humidity flux, and scalar fluxes are approximately linear.

The mixed layer reaches a depth ranging from a few hundred to a few thousand meters by late afternoon. Its top is marked by a sharp increase in temperature within the interfacial layer, where warmer and dryer air from the free atmosphere is entrained into the mixed layer. Entrainment (see its numerical simulation at[10]) is caused by updrafts which impinge the stably stratified free-atmosphere and originate local inflows of air into the mixed layer (e.g., Sullivan et al, 1998). Due to the entrainment, the mixed layer can deepen at a rate of a few tens of centimeters per second. This deepening can be limited by a large scale subsidence or thermal advection.

Convection in the shearless mixed layer (no wind) is organized in a characteristic cell pattern, depicted in Figure 23. In the figure, areas of faster updrafts (shaded areas) are surrounded by areas of slowly sinking air. Downdrafts cover more than half the area of the horizontal plane over the bulk of the mixed layer depth. The presence of wind breaks the cells and replaces them with horizontal rolls**,** often marked by cloud patterns at the top (as depicted in Figure 12).

The structure of the convective boundary layer has been extensively investigated during the last four decades (e.g., Ball, 1960; Lilly, 1968; Betts, 1973; Tennekes, 1973; Deardorff, 1974 b; 1976; 1979; Zeman and Tennekes, 1977; Mahrt, 1979).

[10] http://www.mmm.ucar.edu/asr96/sullivan1.html

As a result, simple mixed-layer models have been developed. To explain this approach, we will refer to Figure 24.

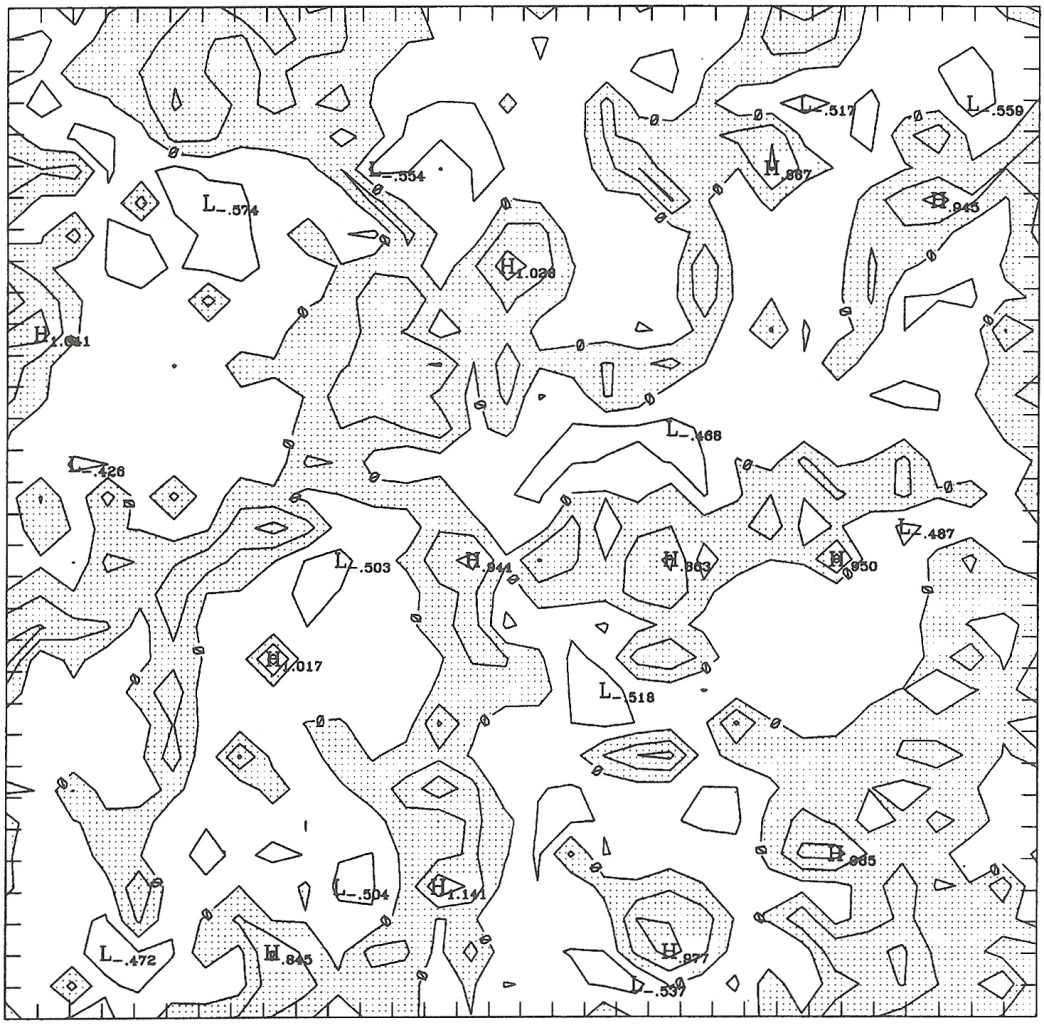

Figure 23. Horizontal cross-section of the vertical velocity field at $z/z_i = 0.3$ based on a large-eddy simulation. Contours plotted from -0.4 m s^{-1} to 0.8 m s^{-1} by 0.4 m s^{-1}. The shaded areas indicate updrafts (after Sorbjan, 1997).

In Figure 24, two profiles of the potential temperature in the mixed layer are depicted in Figure 24. Subscripts "1" and "2" in the figure refer to time instants $t = t_1$ and $t = t_2$. The mixed layer height z_i is defined as a level of the minimum heat flux H. The potential temperature in the mixed layer (above the surface layer) is constant with height. There is a rapid increase in the virtual potential temperature $\Delta\Theta$ in the interfacial layer, which is assumed to be very thin (usually, it is about 100-200 m deep). In the free atmosphere, the potential temperature gradient Γ is assumed to be constant. Note that there is a rapid increase in the wind speed at the top of the mixed layer.

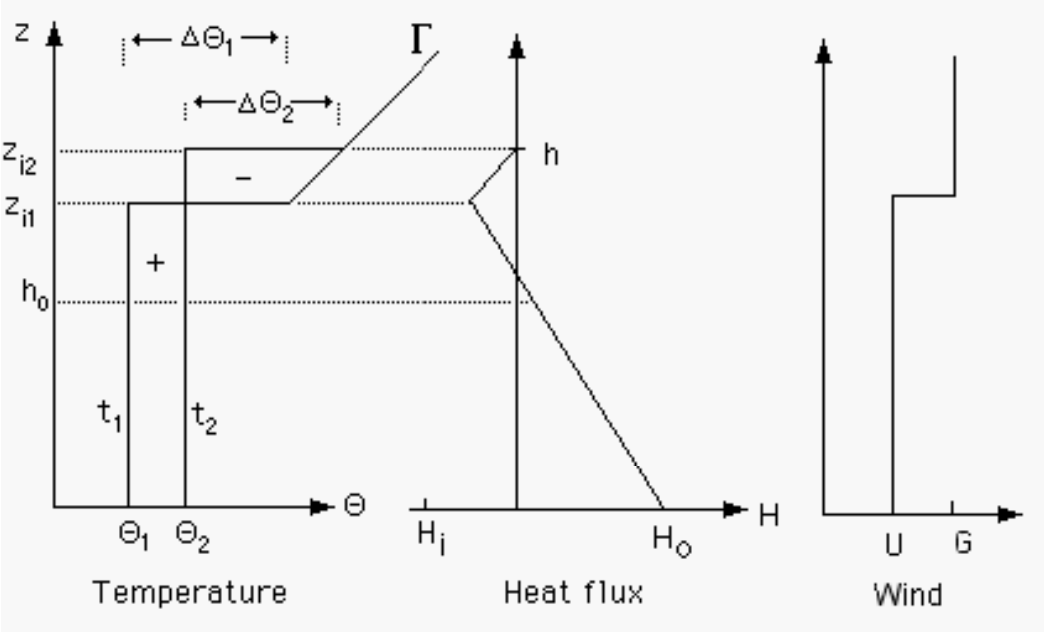

Figure 24. Schematic profiles of the virtual potential temperature, its flux and the wind velocity in the cloud-free mixed layer (G is the geostrophic wind).

The temperature changes in the mixed layer can be expressed by the following, horizontally-averaged equation (e.g., Sorbjan 1995):

$$\partial\Theta/\partial t = -\partial H/\partial z \tag{29}$$

where Θ is the potential temperature and H is the horizontally averaged turbulent heat flux.

Averaging this equation within an interval from t_1 to t_2 yields:

$$\delta\Theta/\delta t = -\partial H/\partial z \tag{30}$$

where $\delta\Theta = \Theta_2 - \Theta_1$, $\delta\tau = \tau_2 - \tau_1$, and H is the temporal and horizontal average of the turbulent heat flux. Integrating (30) with respect to z, we obtain:

$$H(z) = H_o - \int_o^z \delta\Theta/\delta t \, dz \tag{31}$$

Since $\delta\Theta/\delta t$ is positive and constant with height in the mixed layer, we see that the heat flux has to linearly decrease with height from H_o to the most negative value $H_i = H_o - z_i\delta\Theta/\delta t$, *at* $z = z_i$.

From (31) it follows that the area between the temperature profiles $\Theta(t_1)$ and $\Theta(t_2)$, but below $z = h_o$, equals to $H_o \delta t$. Therefore, it represents the heating of the mixed layer by the positive heat flux at the Earth's surface.

The area between the same profiles in the layer between $z = h_o$ and $z = z_{i1}$ (marked as "+" in Figure 23) is equal to H_i. Thus, it indicates the heating of the mixed layer by entrainment at the top of the mixed layer. The area between the temperature profiles in the layer between $z = z_{i1}$ and $z = h$ (marked as "-" in Figure 23) represents the cooling of the inversion layer by thermals:

$$H_i = -\int_{h_o}^{z_{i1}} \delta\Theta/\delta t \; dz = \int_{z_{i1}}^{h} \delta\Theta/\delta t \; dz \tag{32}$$

From Figure 24, and from (32), we can also obtain that:

$$H_i = \int_{z_{i1}}^{h} \delta\Theta/\delta t \; dz = -(z_{i2} - z_{i1})/\delta t \; [\Delta\Theta_2 - \Gamma(z_{i2} - z_{i1})/2] \approx -dz_i/dt \; [\Delta\Theta - \Gamma dz_i/dt \; \delta t/2] \tag{33}$$

where we assumed that $(z_{i2} - z_{i1})/\delta t \approx dz_i/dt$. When $\Gamma dz_i/dt \; \delta t/2$ is small, the result coincides with the result derived analytically by Lilly (1968) by using Leibnitz's rule, $H_i = -dz_i/dt \; \Delta\Theta$. When subsidence w_s is present, its value has to be subtracted from the entrainment rate dz_i/dt. The typical value of H_i/H_o is -0.2 for Γ about 3K/km. Wind shear increases this value to $-(0.2 + u_*^3/w_*^3)$ (e.g., Moeng and Sullivan 1994, Sullivan at al., 1998).

From Figure 24, we will also obtain that $\Delta\Theta_2 = \Delta\Theta_1 - (\Theta_2 - \Theta_1) + \Gamma(z_{i2} - z_{i1})$, which yields in the limit of $\delta t \to 0$:

$$d(\Delta\Theta)/dt = \Gamma dz_i/dt - d\Theta/dt \tag{34}$$

The obtained expression indicates that (in absence of subsidence) $\Delta\Theta$ increases in time as z_i grows and decreases as the temperature in the mixed layer increases. The above formula was first obtained by Betts (1973).

2.5.3 Self-Similar Structure of the Mixed Layer

Deardorff (1970 a, b) noted that the in the core portion of a quasi-steady mixed layer, turbulence has a self-similar structure, described by the following convective scales:

$$\begin{aligned} &z_i \text{ for height,} \\ &w_* = (z_i\, \beta\, H_o)^{1/3} \text{ for velocity,} \\ &\Theta_* = H_o/w_* \text{ for temperature,} \\ &q_* = Q_o/w_* \text{ for humidity,} \end{aligned} \tag{35}$$

where z_i is the mixed layer height, H_o and Q_o are the surface temperature and humidity fluxes, and $\beta = g/T_o$ is the buoyancy parameter. Consequently, the statistical moments of turbulence (i.e., variances, covariances, etc) were implied by him to be functions of only z/z_i, when non-dimensionalized by these scales. The general form of such functions, however, has not yet been found.

Measurements showed, however, that in the upper portion of the mixed layer, a substantial scatter of dimensionless quantities exists. This scatter indicated that the list of scales provided by Deardorff was incomplete in this region. Large-eddy simulation performed by Sorbjan (1996 a, b) demonstrated that the statistical moments involving temperature are strongly sensitive to changes of the potential temperature gradient in the free-atmosphere Γ. On the other hand, the moments involving only the vertical velocity were found practically independent of Γ. The ratio $R = - H_i/H_o$ of the heat fluxes at the top and bottom of the mixed layer was found to increase when Γ increased. For the values of Γ from 1 K/km to 10 K/km, typically observed in the atmosphere, the heat flux ratio R varied in the range 0.2 to 0.3. When Γ decreased to zero, the heat flux H_i at the top of the mixed layer also decreased to zero.

Further investigations revealed that the appropriate scales at the top of the shear-free convective atmospheric boundary layer (no mean wind) are (Sorbjan, 2003):

$$\begin{aligned} &w_* N/\beta \quad \text{for temperature,} \\ &w_* \quad \text{for velocity,} \\ &N^{-1} \quad \text{for time,} \\ &w_*/N \quad \text{for height,} \end{aligned} \tag{36}$$

where N is the Brunt-Vâisâlâ frequency in the interfacial layer, $N = [\beta\, \gamma_i]^{1/2}$, γ_i is the potential temperature gradient in the interfacial layer, and β is the buoyancy parameter.

The presence of two different regimes, in the core of the mixed layer and at its top, with two different sets of scales, makes formulating the similarity functions very difficult. One might suspect, however, that such functions should be expressed in terms of two components F_1 and F_2:

$$m_s = F_1\,(z/z_i) + F_2\,(z/z_i, \ldots) \tag{37}$$

where m_s is the dimensionless moment, scaled in terms of (35), F_1 is the universal function dependent only on the dimensionless height z/z_i, and F_2 is the correction due to entrainment, expressed in terms of z/z_i, as well as the scales (35) and (36).

In the shearless case, the function F_2 is expected to be non-zero only for moments involving temperature. For example for the heat flux $H(z)$ and for the temperature variance σ_θ^2, one might propose:

$$H/H_o = (1 - z/z_i) + c\ w_* N / (\beta\Theta_*)\ \ z/z_i \tag{38}$$

$$\sigma_\theta^2 / \Theta_*^2 = c_1 (1 - z/z_i)^{4/3} / z/z_i^{2/3} + c_2 (w_* N)^2 / (\beta\Theta_*)^2\ \ z/z_i^{4/3} / (1 - z/z_i + c_3)^{4/3}$$

where H_o is the surface heat flux ($H_o = w_*\Theta_*$), and c, c_1, c_2, c_3 are empirical constants.

The presence of wind shear introduces further complications. In this case, characteristics of turbulence at the top of the mixed layer seem to be dependent not only on the temperature gradient, but also on velocity gradients. As a result, function F_2 in (37) will be dependent on an additional variable Ri^{-1}, where Ri is the Richardson number, defined as:

$$Ri = \beta\, d\Theta/dz / [(du/dz)^2 + (dv/dz)^2] \tag{39}$$

and β is the buoyancy parameter. In this case, the function F_2 is expected to be non-zero for all moments. Note, that when $Ri \to \infty$ (the shearless case), $Ri^{-1} \to 0$, and the dependence of F_2 on Ri vanishes (Sorbjan, 2001, 2003).

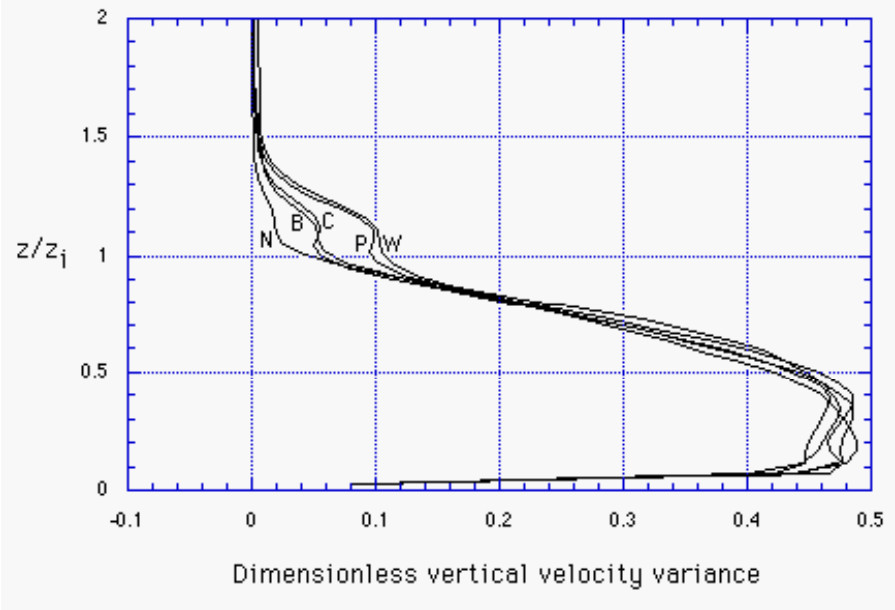

Figure 25. The vertical velocity variances scaled by w_*^2, for five LES runs: B - barotropic case ($s_x = 0$, $s_y = 0$), W-warm advection ($s_x = 0$, $s_y = -5$), C-cold advection ($s_x = 0$, $s_y = 5$), P-positive shear ($s_x = 5$, $s_y = 0$), N - negative shear ($s_x = -5$, $s_y = 0$), where $s_x = du_g/dz$, $s_y = dv_g/dz$ are the components of the geostrophic shear, expressed in m/s per km (after Sorbjan, 2003)

Figure 25 shows profiles of the vertical velocity variance, scaled by w_*^2, in the boundary layer with wind shear. The profiles were obtained based on a numerical model (LES), for the surface geostrophic wind G_o = 15 m/s, and for five different values of a geostrophic shear in the atmosphere (Sorbjan, 2003).

2.5.4 Decaying Mixed Layer

Eventually in the late afternoon, the surface heat flux H_o begins to weaken in response to the decreasing sun's elevation. As a result, the turbulent time scale $t_* = z_i / w_*$ increases (because w_* decreases and z_i stays nearly constant), and becomes comparable with the forcing time scale (a few hours). From this moment, quasi-stationarity and convective similarity disappear.

A numerical study of the decaying atmospheric convective mixed layer, caused by a gradual shut-off of the upward surface heat flux, was performed by Sorbjan (1997). It indicated that during decay, turbulent eddies persist even when the heat flux at the surface becomes negative, and the surface inversion develops near the Earth's surface. Large-scale updrafts are able to penetrate the stable layer aloft and cause entrainment from the capping stable layer. The resulting profiles of the heat flux are depicted in Figure 26. The x-y cross-section of the vertical velocity in the decaying mixed layer is shown in Figure 27.

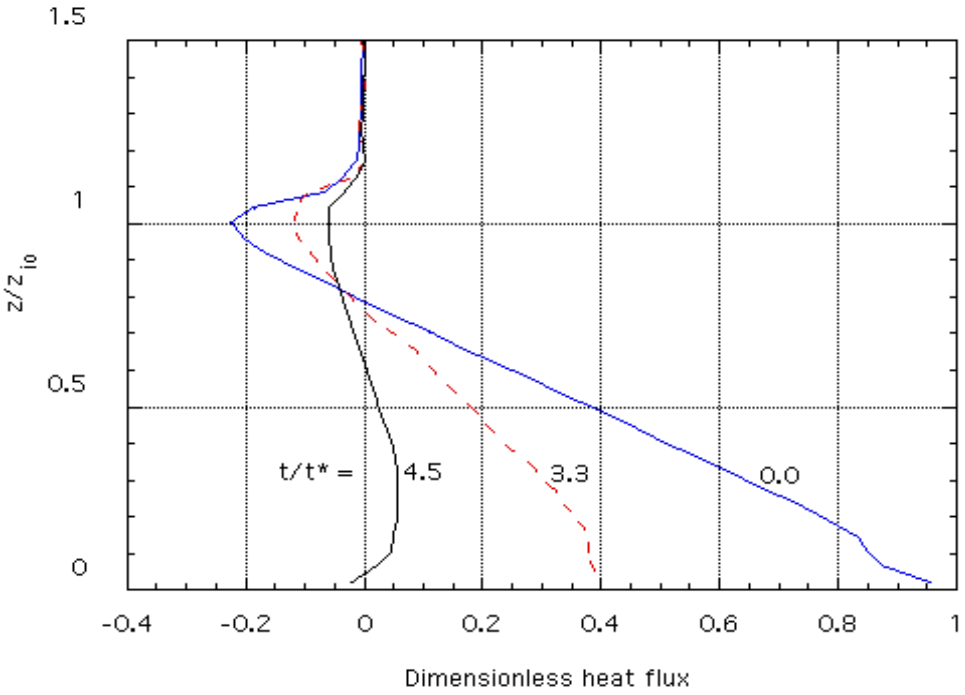

Figure 26. Profiles of the dimensionless heat fluxes in the decaying mixed layer, scaled by the surface heat flux at t/t* = 0.0 (a large-eddy simulation of Sorbjan, 1997).

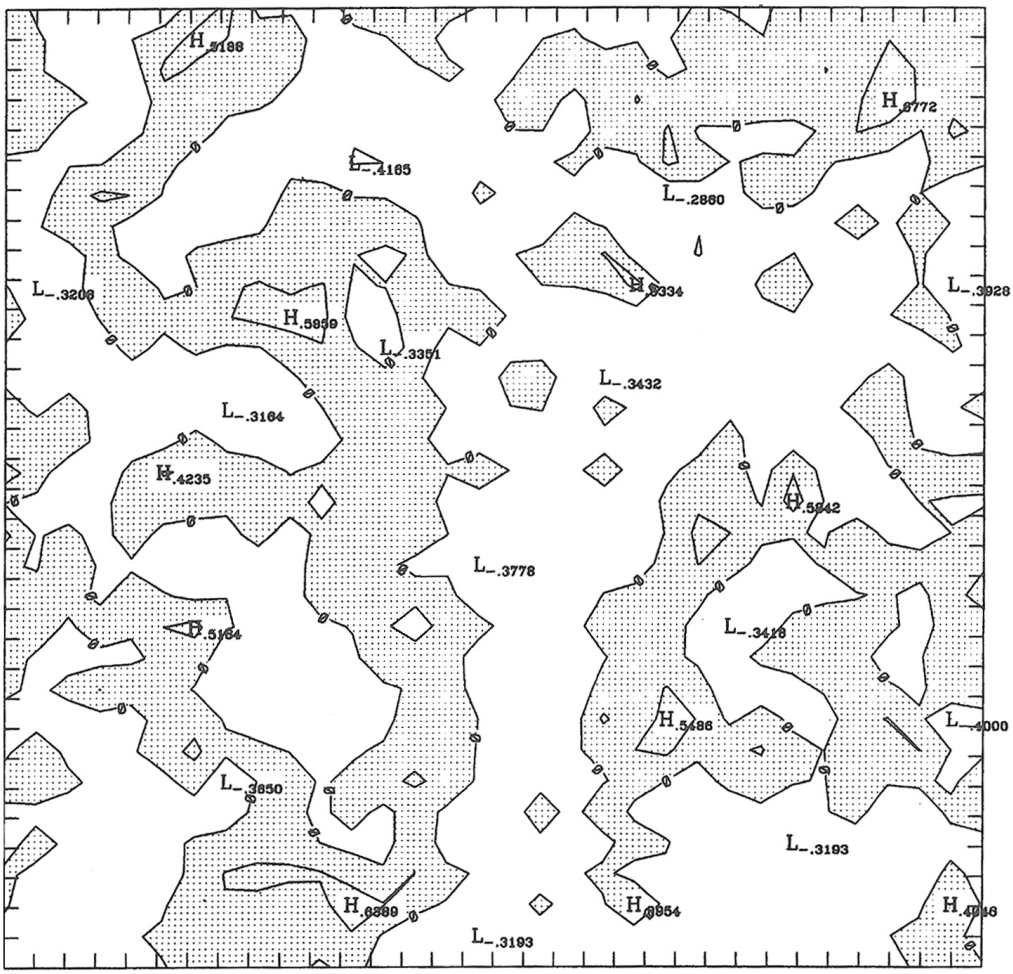

Figure 27. Horizontal cross-section of the vertical velocity field at z/z_i= 0.3 during decaying convection, t/t_*=4.5, based on a large-eddy simulation. Contours plotted from -0.4 m s^{-1} to 0.8 m s^{-1} by 0.4 m s^{-1}. The shaded areas indicate updrafts (after Sorbjan, 1997).

Figure 26 was plotted for $z/z_i = 0.3$, and at $t/t_* = 4.5$. At $t/t_* = 4.5$, the heat flux at the surface is already negative. Nevertheless, convective cells are still present in Figure 27. Even though the vertical motions are weakened, the structure of the largest eddies seem almost unchanged with respect to the initial state in Figure 23.

2.5.4 Diffusion in the Mixed Layer

The understanding of diffusion associated with point sources located within the mixed layer was significantly advanced by the numerical simulations of Deardorff (1972) and Lamb (1982), as well as the laboratory experiments of Willis and Deardorff (1976, 1978, 1981). Their investigations indicated that for elevated sources the average plume center-line, defined as the mean maximum concentration, descended within a short distance from the source until it reached the ground. In contrast, the average centerline from near surface releases ascended after a short downwind distance (see Figure 28).

Figure 28 shows averaged and cross-wind integrated concentrations released from two sources. The first source is located near the surface while the second one is elevated. The figure indicates that the locus of the maximum concentrations ascends with a distance from the source for the case of the first source. In the second case, the locus of the maximum concentrations first descends, reaches the Earth's surface and then ascends. The presented results indicate that the obtained patterns differ from those produced by the Gaussian plume models.

This rather surprising plume behavior has been the subject of many subsequent studies. The main objective was not only to offer a physical explanation, but also to improve simpler diffusion models which had failed in this particular case. The first support for Willis and Deardorff's laboratory observations was obtained from the numerical experiments of Lamb (1982). Lamb used the results from the LES model of Deardorff (1972) to trace the motions of thousands of particles released into a numerical field. Later, other types of particle models were successfully employed in simulating convective plume behavior (e.g., Misra, 1982; Baerentsen and Berkowicz, 1984; Sawford and Guest, 1987). The laboratory observations also agreed with the atmospheric diffusion data (e.g., Moninger et al., 1982; Eberhart et al., 1988).

It soon became clear that the position of maximum concentrations could be explained by the probability distributions of the vertical velocity. Distributions of the vertical velocity in the clear-sky convective boundary layer were found to be positively skewed with a negative mode (e.g., LeMone, 1990). A positive vertical velocity skewness indicates strong narrow updrafts surrounded by larger areas of weaker downdrafts, as depicted in Figure 23. It also implies that downdrafts cover more than half the area of the horizontal plane over the bulk of the mixed layer depth. As a result, the majority of material released by an elevated source starts descending and continues to descend for a significant amount of time. On the other hand, material released at the surface can only ascend or move horizontally. Contaminants released into the base of an updraft begin to rise immediately, while those emitted into a downdraft move approximately horizontally until they encounter updrafts, and are transferred upward. After a sufficiently long travel time, in which a majority of pollutants enter the updrafts, the location of the maximum concentration lifts off the ground and rises toward the top of the mixed layer.

We shall now discuss the diffusion of passive species (such as humidity, ozone, radon, and carbon dioxide) which are associated with area sources (or sinks) located at the Earth's surface, and at the top of the mixed layer. Dispersion of such species in the mixed layer can be described by the following equation:

$$\partial c/\partial t = - \partial Q/\partial z \qquad (40)$$

where c is the concentration, and Q is the concentration flux.

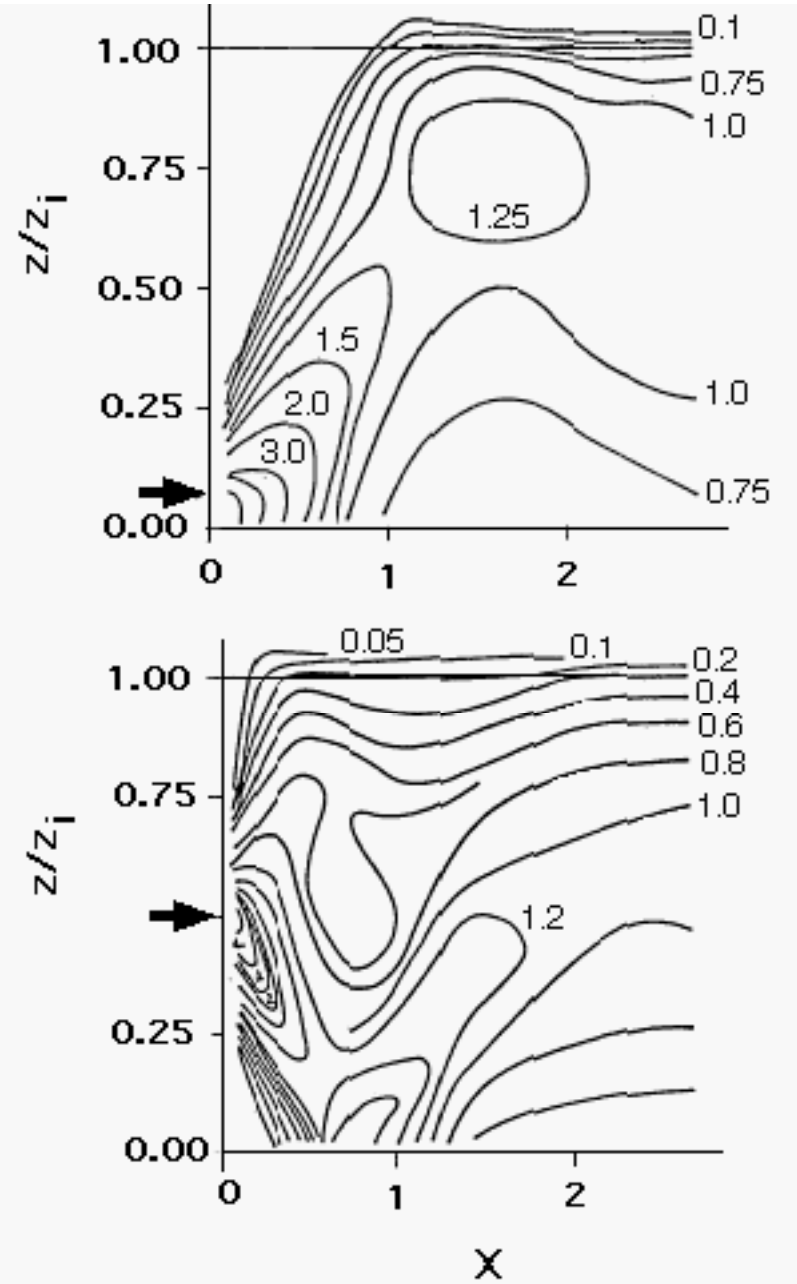

Figure 28. Vertical concentration distributions as a function of non-dimensional dispersion distance $X = w_* x/(Uz_i)$ for a low and high-level sources (after Willis and Deardorff, 1976 and 1982).

When the scalar is "well mixed", the concentration flux Q is a linear function of height: $Q(z) = Q_o\ (1\text{-}z/z_i) + Q_i\ z/z_i$ where Q_0 is the turbulent flux at the surface, Q_i is the turbulent flux at $z = z_i$. Due to linearity of (40) with respect to c and Q, the mixing of a passive scalar in the mixed layer is additive, i.e., it can be expressed as a superposition of two processes, "bottom-up" and "top-down" (e.g., Wyngaard, 1984).

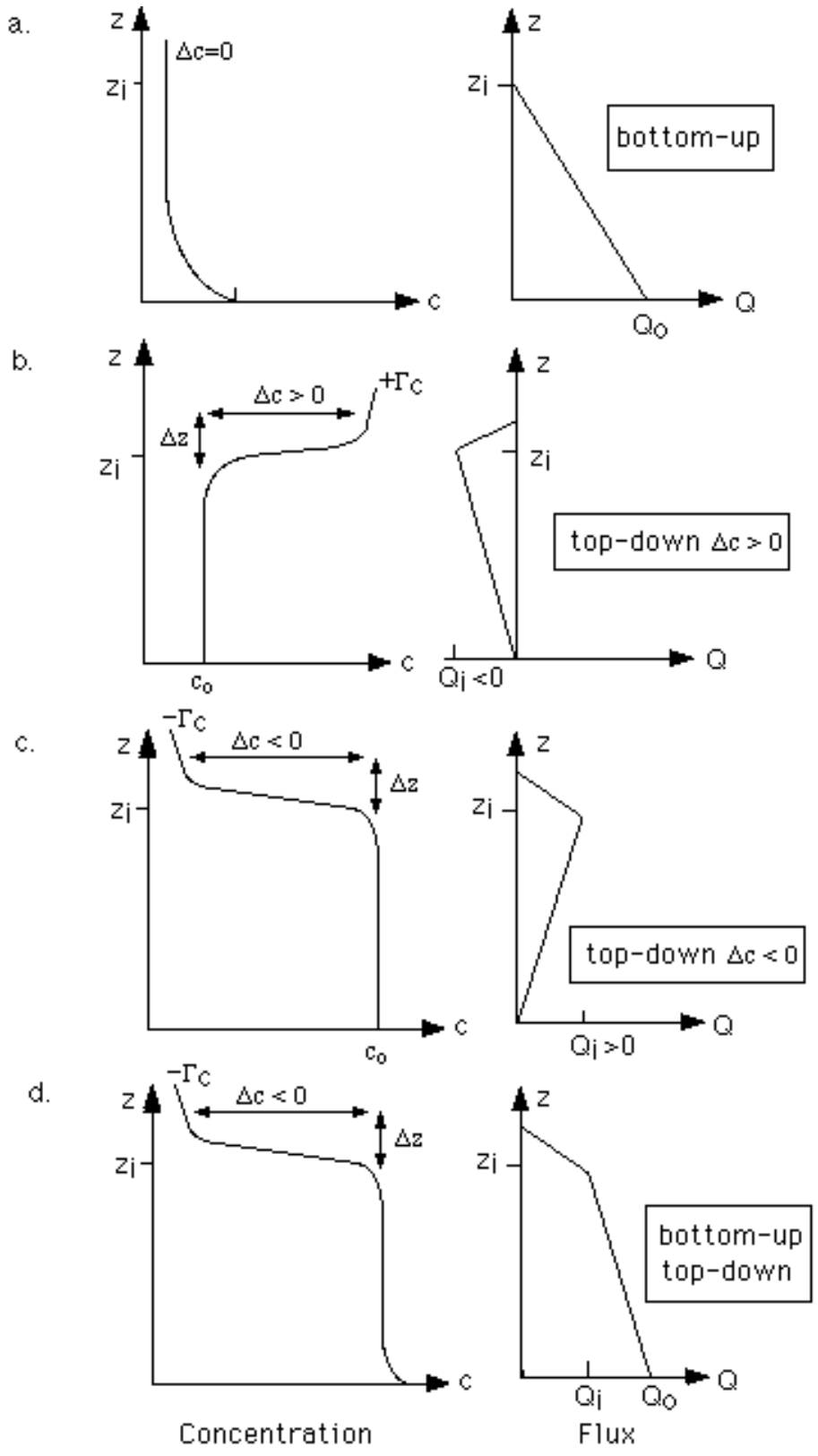

Figure 29. Bottom-up and top-down diffusion in the mixed layer for a passive scalar emitted from a surface source (after Sorbjan 1999a).

The first process (hereafter denoted by subscript "b") is associated with a transfer (emission or absorption) of a scalar across the Earth's surface.The second process (hereafter denoted by subscript "t") is due to entrainment of a scalar at the top of the mixed layer. Consequently, the mean concentration of the passive scalar and its flux can be decomposed as: $c = c_b + c_t$, $Q = Q_b + Q_t$.

The considered diffusion processes are schematically shown in Figure 29**.** In the pure "bottom-up" case (Figure 29a), the concentration quickly decreases with height and reaches a constant value in the mixed layer. At the same time, the "bottom-up" concentration flux decreases linearly from $Q_o > 0$ at the Earth's surface to zero at the top of the mixed layer. In the pure "top-down $(\Delta c > 0)$" case (Figure 29b), the concentration in the free atmosphere exceeds the concentration in the mixed layer. The scalar flux decreases linearly with height, from zero at the surface to $Q_i < 0$ at the top of the mixed layer.

On the other hand, during a pure "top-down $(\Delta c < 0)$" case (Figure 29c), the concentration in the mixed layer is larger than the concentration in the free atmosphere, and the flux increases linearly with height, from zero at the surface to $Q_i > 0$ at the top of the mixed layer.

Diffusion of a passive scalar in Figure 29d $(\Delta c < 0,\ Q_o > Q_i > 0)$ can be represented by a sum of two processes: pure "bottom-up" $(\Delta c = 0,\ Q_o > 0)$ as in Figure 29a, and pure "top-down" $(\Delta c < 0,\ Q_o = 0,\ Q_i > 0)$ as in Figure 29c. A superposition of processes in Figures 29b and 29c yields a constant concentration (equal to $2c_o$), and a zero concentration flux in the mixed layer, and also above.

2.6 Cloud-Topped Mixed Layers

Even though stratocumuli clouds have a strong impact on the dynamics of the PBL (e.g., Lenschow et al. 1980, Betts 1990, Betts and Boers 1990, Siems et al. 1990, Nichols and Leighton 1986, Turton and Nicholls 1987, Chai and Telfort 1983, Telfort and Chai 1984, Agee and Hart 1990, Moeng and Schumann, 1991, Paluch and Lenchow 1991), their effects are usually neglected in air pollution studies.

The structure of the cloud-topped boundary layer (CTBL) depends on radiative cooling and heating in clouds, phase changes, subsidence, sensible and latent fluxes, and wind shear. Surface fluxes generate convection and provide the water substance. Radiative cooling contributes to the generation of a positive heat flux, convection, and entrainment at the top of the mixed layer. Wind shear increases entrainment. Entrainment brings warmer and drier air down into the ABL and promotes evaporative cooling. The evaporative cooling may lead to an instability process in which parcels cool even more and then sink. This can generate greater entrainment, resulting in the breaking up of a solid cloud deck.

Mixed layer convection requires a source of energy. In the cloud-free mixed layer, the energy is provided by the heated Earth's surface. The presence of stratocumuli clouds introduces additional buoyancy sources and sinks through radiative cooling and heating and evaporative cooling. The shortwave heating is smaller than the longwave cooling, and is distributed over a thicker layer within a cloud. Due to radiative and evaporative cooling the depth of the interfacial layer is very thin and the temperature jump quite large. Numerical simulations (e.g., Lock and MacVean, 1999, Krueger et al, 1995) show that thermals hindering on the inversion interface are flattened and only slightly deform the interface. They spread out horizontally, generating enhanced shears at the interface and small-scale Kelvin-Helmholtz type mixing.

The day-time CTBL has two distinct layers, cloud and subcloud layer, decoupled by the formation of a slightly stable layer near the cloud base. The decoupling is primarily a consequence of the shortwave heating in the cloud layer. The decoupling prevents the moisture from being transported upward. This leads to a rapid thinning of the cloud layer during the daytime, and also has an important influence on the radiative balance at the Earth's surface. In addition, cooling introduced by the evaporation of drizzle can cool the sub-cloud layer relative to the cloud layer, and consequently can further stabilize the interface between the cloud and sub-cloud layers.

A physical description of the cloud-topped boundary layer is more complex than in the dry case considered above. In a cloud-topped mixed layer, the virtual potential temperature is no longer a conservative variable (Figure 30). Instead, the liquid water potential temperature:

$$\Theta_L = \Theta - L/c_p \, q_L \tag{41}$$

can be considered as an invariant in moist adiabatic processes, where L is the latent heat of evaporation, c_p is the specific heat of air at constant pressure, q_L is the liquid water mixing ratio (e.g., Moeng, 1998).

To illustrate the impact of clouds in this section we will modify the analysis presented in section 2.5.2 by assuming that stratocumuli clouds are present on the top of the PBL. We will consider only a nocturnal (no solar radiation), horizontally homogeneous, cloud-topped mixed layer, schematically depicted in Figure 31.

In a cloud-topped mixed layer, the liquid water potential temperature Θ_L is approximately constant with height. At the top of the mixed layer, there is a sudden jump in the liquid water potential temperature $\Delta\Theta_L$ ($\Delta\Theta_1$ *at* $t = t_1$ and $\Delta\Theta_2$ *at* $t = t_2$). The temperature jump takes place in the transition layer of very small depth, which could be in the order of 10 m thick or even less. Consequently, we will assume here that the transition layer is infinitesimal in Figure 31. Above the

mixed layer the liquid water potential temperature gradient Γ is assumed to be constant. The value of the surface heat flux is assumed to be near zero.

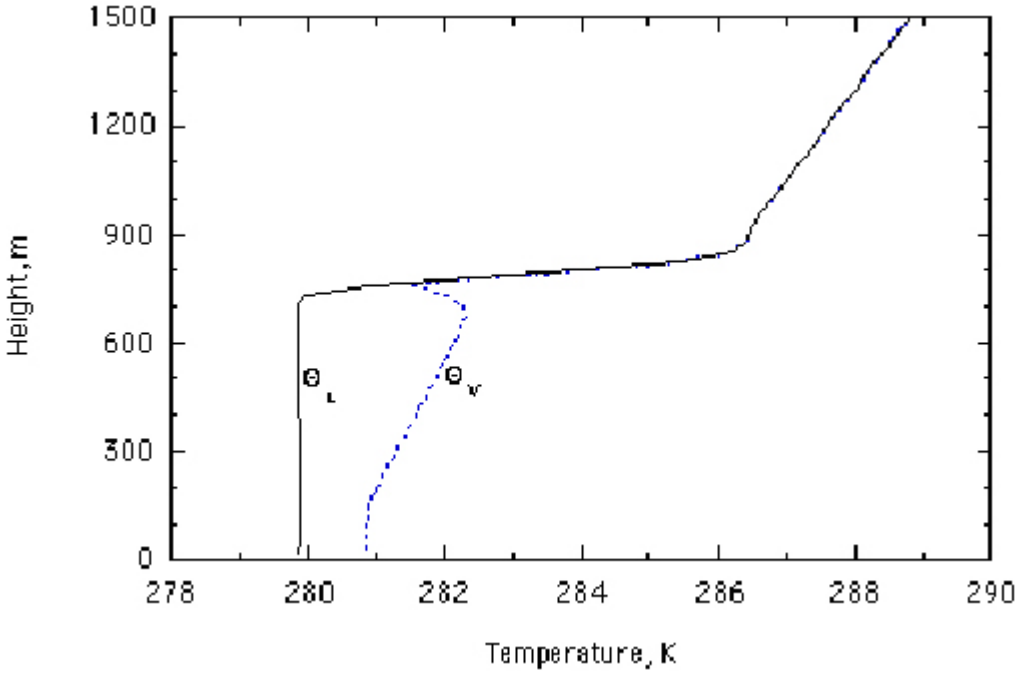

Figure 30. Typical vertical profiles of the liquid water potential temperature Θ_L, and the virtual temperature Θ_v in the cloud-topped boundary layer (a large-eddy simulation of Sorbjan and Uliasz, 1999b).

The liquid water potential temperature changes in the mixed layer can be expressed by the following time-averaged equation:

$$\delta\Theta_L/\delta t = -\partial F/\partial z \tag{42}$$

where, $\delta\Theta_L = \Theta_2 - \Theta_1$, F is the time and horizontally-averaged total flux, which consists of the liquid water potential temperature heat flux H_L, and the net radiative flux R, i.e., $F = H_L + R$. Integrating (42), we obtain:

$$F(z) = F_o - \int_o^z \delta\Theta_L/\delta t \; dz \tag{45}$$

Referring to Figure 31, we can note that since $\delta\Theta_L/\delta t$ is negative and constant with height in the mixed layer, the total heat flux linearly increases with height, from F_o at the Earth's surface to $F_i = F_o - z_i\delta\Theta_L/\delta t$, at $z = z_{i1}$. Above $z = z_{i1}$, the total heat flux is non-linear.

We will assume that the mean radiative flux R increases with height from zero at $z \leq h_r$ *to* R_a *at* $z = h = z_{i2}$. The turbulent temperature flux can be obtained as the

difference between the total and radiative fluxes, $H_L = F - R$. Below $z = h_r$, $R = 0$, and consequently H_L is linear, $H_L = H_o - \delta\Theta_L/\delta t\ z$. H_L is non-linear for $z>h_r$. At $z = h_o$, where the radiative flux R and the total flux F are equal, and H_L is nil. At $z = z_m$, where the difference between R and F is the greatest, and H_L is the most negative. At $z = h$, H_L is zero again. The area between curves $\Theta_L(t_1)$ and $\Theta_L(t_2)$, below $z = h_r$ (where $R = 0$), represents the cooling of the mixed layer by the positive heat flux H_L. The area between profiles $\Theta_L(t_1)$ and $\Theta_L(t_2)$ above $z = h_r$ (where $R \neq 0$) represents the direct radiative cooling of the mixed layer.

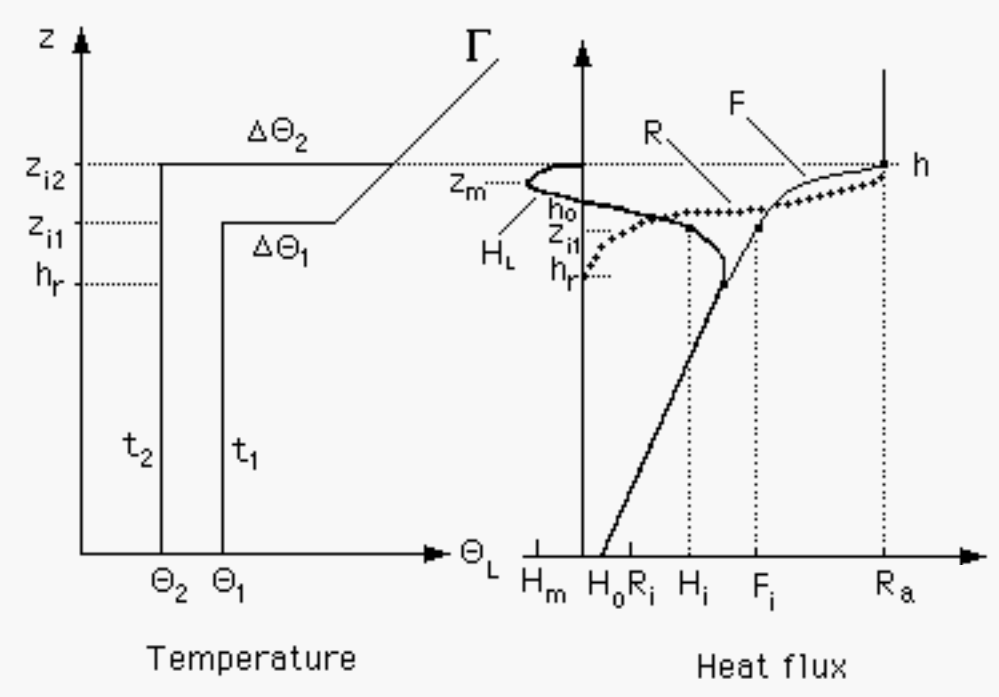

Figure 31. Schematic profiles of the liquid water potential temperature and its flux in the cloud-topped nocturnal mixed layer

The above analysis indicates that the presence of stratocumuli clouds above the boundary layer generates a positive heat flux, convection and mixing in nocturnal conditions. The numerical diffusion simulations performed by Sorbjan and Uliasz (1998) demonstrated that vertical mixing in the nocturnal cloud-topped boundary layer is non-Gaussian, resulting from the negatively skewed vertical velocity field in most of the layer.

2.7 Stability Categories

The structure of the atmospheric boundary layer is quite complex to non-meteorologists. Therefore, a simplifying alternative proposed over 40 years ago by Pasquill (1961) has been very popular since then among engineers dealing with air-pollution problems.

Pasquill's classification of weather conditions in the boundary layer is based on five stability categories. The key to these categories are described in the following table:

Table 2. Pasquill's Stability Categories

Surface Wind Speed (m/s)	Daytime Insolation			Nighttime cloud cover	
	Strong	Moderate	Slight	Thinly overcast or ≥ 4/8 low cloud	≤ 3/8
< 2	A	A - B	B	-	-
2 - 3	A - B	B	C	E	F
3 - 5	B	B - C	C	D	E
5 - 6	C	C - D	D	D	D
> 6	C	D	D	D	D

According to Pasquill, strong insolation is equivalent to a sunny midday in summer in England and slight insolation to conditions in midwinter. The neutral category *D* corresponds to overcast conditions during day or night, and sky conditions during the hour preceding or following night (Pasquill's night begins 1 hour before sunset and lasts to 1 hour after dawn), regardless of wind speed. The categories *A* and *F* have traditionally been associated with very unstable and very stable conditions.

Our understanding of the boundary layer has progressed since the 1960's, when Pasquill's classification was proposed. Therefore, today his stability categories could be refined as follows:

A. free-convection with or without cumulus clouds,
B. forced-convection with or without cumulus clouds,
C. weaker day-time convection,
D. very weak or no convection during daytime, nighttime, or day-night transitions,
E. weak stable nocturnal regime with thin low clouds or with medium clouds,
F. strong stable conditions under clear skies.

As correctly indicated by Pasquill (1961) dispersion of pollutants in the atmosphere strongly depends on meteorological conditions. The vertical appearance of an instantaneous plume offers considerable information as to how the thermal and dynamic state of the lower atmosphere influences the transport of atmospheric pollutants. Some idealized patterns of vertical smoke spreading can be identified as looping, fumigation, lofting, coning, and fanning,. The listed cases are briefly discussed below.

"Looping" is frequently evident by midday in the mixed layer (Figure 32). It can be identified as category *A, B* or *C*. In this case convection generates large eddies which bring the plume to the ground and also lift it upward. This causes the

looping behavior and intense turbulent mixing. The average ground-level concentration increases very rapidly with distance from the stack, attains its peak value and then decreases farther downwind

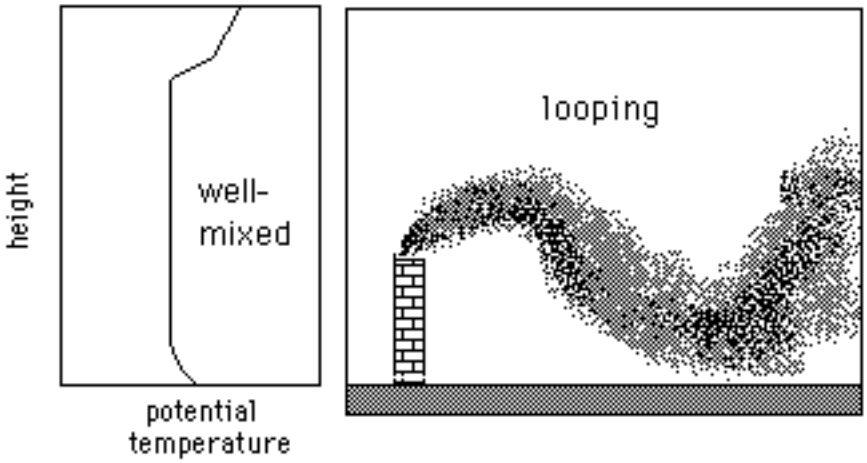

Figure 32. The looping conditions in the well-mixed layer.

The second case is called "fumigation" (Figure 33). Shortly after the sun rises on a clear morning, the existing nocturnal inversion begins dissipating and is slowly replaced by the mixed layer. The inversion layer is present just above the top of the stack and acts as a lid. The newly developed convective eddies spread the pollutants within the mixed layer. It causes a sudden rise in ground-level concentrations. Depending upon the stack height and the deepening-rate of the inversion layer, the fumigation condition may be very transitory or could persist for several hours. The case should be identified as category *A, B,* or *C*.

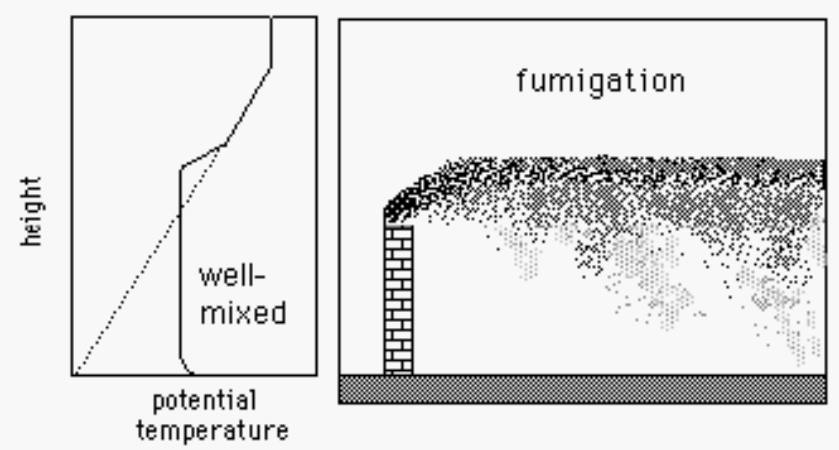

Figure 33. The fumigation conditions in the evolving morning mixed layer.

"Coning" usually accompanies cloudy conditions, with moderate winds and with very weak convection (Figure 34). It can occur either during the day or night. Therefore is should be identified as category *D*. In this case the plume is shaped

like a cone with a horizontal axis. The distance from the stack at which the smoke first comes to the ground is greater than it would be in looping conditions because the thermally induced turbulence is lower in this case.

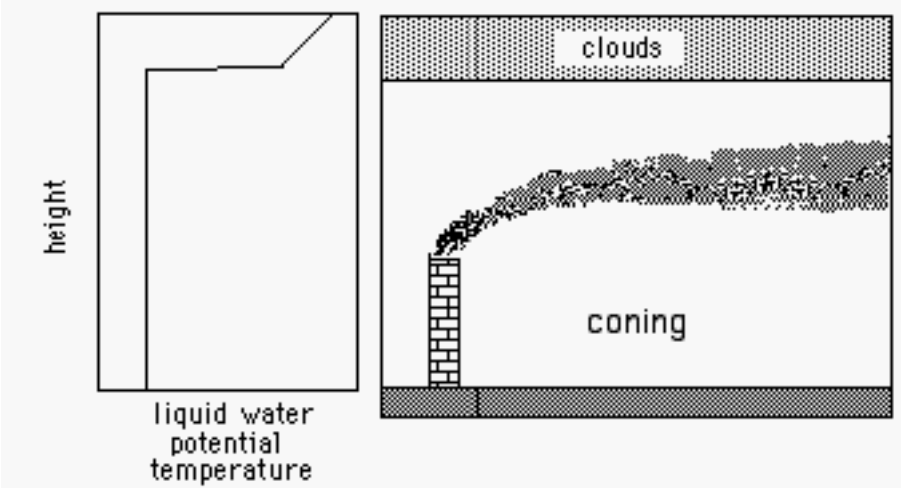

Figure 34. The coning conditions in the cloud-topped boundary layer.

"Lofting" is most often observed near sunset (Figure 35). It should be identified as categories *E* or *F*. When the surface inversion is developed just below the top of the stack, it reduces diffusion downward. At the same time, eddies in the residual mixed layer can still be active and cause intensive diffusion above the surface inversion,. Depending upon the stack height and the deepening-rate of the inversion layer, the lofting condition may be very transitory or could persist for several hours. When the source is above the surface inversion, lofting may be the most favorable condition.

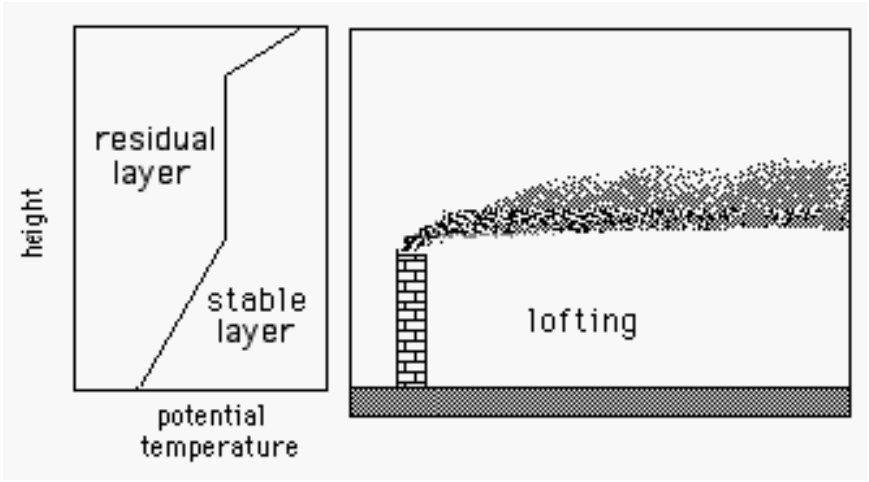

Figure 35. The lofting conditions during evening or nocturnal conditions.

The so called "fanning" occurs at night in the stable PBL (Figure 36). Therefore, it can be associated with category *F*. Since vertical mixing is suppressed, the plume expands very little in depth over long distances. Lateral diffusion may proceed quite differently. The slow meandering of the wind results in a similar meandering of the plume. Therefore, the time-averaged plume may appear quite broad. When the horizontal spreading is small, the plume can be observed for long distances. Fanning behavior of plumes is not considered an unfavorable condition for tall stacks. This situation might be unfavorable, however, when the stack is short.

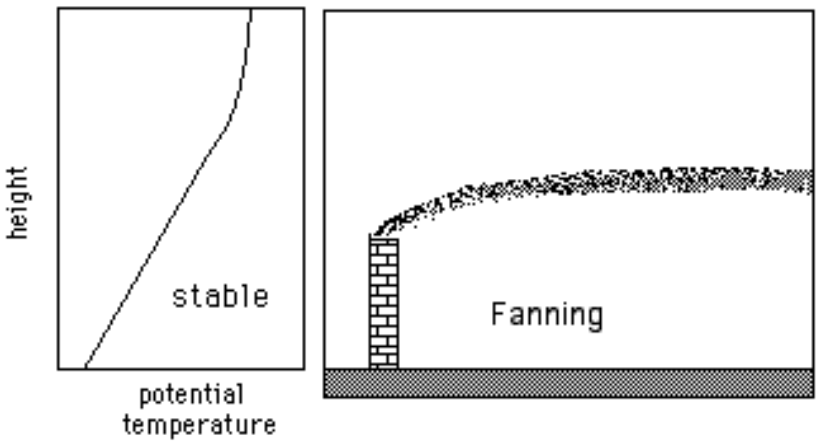

Figure 36. The fanning conditions in the stable boundary layer.

References

Agee, E.M., 1987: Mesoscale cellular convection over the oceans. *Dynamics of Atmospheres and Oceans,* 10, 317-341.

Agee, E.M., and M.L. Hart, 1990: Boundary layer and mesoscale structure over lake Michigan during winter time cold outbreak. *J. Atmos. Sci*., 47, 2293-2316.

Arya, S.P., 1999, Air Pollution Meteorology and Dispersion. Oxford University Press

Atkinson, B.W. 1995: Introduction to the fluid mechanics of meso-scale flow field. In: Diffusion and Transport of Pollutants in Atmospheric Mesoscale Flow Fields. Kluwer Academic Publishers, Eds. Albert Gyr and Franz-S. Rys, 216 pp.

Baerentsen, J.H. and R. Berkowicz, 1984: Monte Carlo simulation of plume dispersion in the convective boundary layer. *Atmos. Envir*., 18, 701-712.

Ball, F.K., 1960: Control of the inversion height by surface heating. *Quart. J. Roy. Meteor. Soc.*, 86, 483-494.

Betts, A.K., 1973: Non-precipitating cumulus convection and its parameterization. *Quart. J. Roy. Meteor. Soc.*, 99, 178-196.

Betts, A. 1990:Diurnal variation of California coastal stratocumulus from two days of boundary layer soundings, *Tellus*, 42A, 302-304.

Betts A.K., and R. Boers, 1990: A cloudiness transition in a marine boundary layer. *J. Atmos. Sci*., 47, 1480-1497.

Brown, R.A., 1980: Longitudinal instabilities and secondary flows in the planetary boundary layer: A review. *Reviews of Geophysics and Space Physics*, 18, 3, 683-697.

Buckingham, E., 1914: On physically similar systems. Illustration of the use of dimensional equations. *Phys. Rev*. 4, 345-376.

Businger, J.A., J.C.Wyngaard, Y.Izumi, and E.F.Bradley, 1971: Flux profile relationships in the atmospheric surface layer. *J. Atmos.Sci.*, 28, 181-189.

Chai S.K., and J.W. Telfort, 1983: Convection model for stratus cloud over a warmwater surface. *Bound.-Layer Meteor*., 26, 25-49.

Deardorff, J.W., 1970 a: Convective velocity and temperature scales for unstable planetary boundary layer and for Rayleigh convection. *J. Atmos. Sci.*, 29, 1211-1212

Deardorff, J.W., 1970 b: Preliminary results from numerical integration of the unstable planetary boundary layers. *J. Atmos. Sci.*, 27, 1209-1211.

Deardorff, J. W., 1972. Numerical investigation of neutral and unstable planetary boundary layer. *J. Atmos. Sci*., 29, 91-115.

Deardorff, J.W., 1974 a: Three-dimensional numerical study of the height and mean structure of a heated planetary boundary layer. *Bound.-Layer Meteor.*, **7**, 81-106.

Deardorff, J.W., 1974b: Three-dimensional numerical study of turbulence in an entraining mixed layer. *Bound.-Layer Meteor.*, **7**, 199-226.

Deardorff, J.W., 1976: On the entrainment rate of a stratocumulus-topped mixed layer. *Quart. J. Roy. Meteor Soc.*., 102, 563-582.

Deardorff, J.W., 1979: Prediction of convective mixed-layer entrainment for realistic capping inversion structure. *J. Atmos. Sci.*, 36, 424-436.

Eberhart, W.L., W.R. Moninger, and G.A. Briggs, 1988: Plume dispersion in the convective boundary layer. Part I: CONDORS field experiment and example measurements. *J. Appl. Meteor*., 27, 5, 600-616

Garratt, J.R., 1992: The Atmospheric Boundary Layer. Cambridge University Press, 316 pp.

Gossard, E. E.and J. H. Richter, 1970. The shape of internal waves of finite amplitude from high-resolution radar sounding of the lower atmosphere *J. Atmos. Sci*., 27, 971-973.

Gossard, E. E., D. R. Jensen and J. H. Richter, 1971. Analytical study of tropospheric structure as seen by high-resolution radar. *J. Atmos. Sci*., 28, 794-807.

Gossard, E. E., J. H. Richter and D. R. Jensen ,1973. Effect of wind shear on atmospheric wave instabilities revealed by FM/CW radar observations. *Boundary-Layer Meteorol*. 4, 113-130.

Hooke, W. H., F. F. Hall and E. E. Gossard, 1973. Observed generation of an atmospheric gravity wave by shear instability in the mean flow of the planetary boundary layer. *Boundary-Layer Meteorol*., 5, 29-41.

Kaimal, J.C., J.C. Wyngaard, D.A. Haugen, O.R. Coté, Y. Izumi, S.F Caughey, and C.J. Readings, 1976: Turbulence structure in the convective boundary layer. *J. Atmos. Sci.*, **33**, 2152-2169.

Kaimal, J.D., R.A. Eversole, D.H. Lenschow, B.B. Stankov, P.H. Khan, and J.A. Businger, 1982: Spectral characteristics of the convective boundary layer over uneven terrain. *J. Atmos. Sci.* 39, 1098-1114.

Kaimal J.C.and J.J.Finnigan, 1994: Atmospheric Boundary Layer Flows. Oxford University Press, 287 pp.

Krueger, S. K., G. T. McLean and Q. Fu, 1995: Numerical simulation of the stratus to cumulus transition in the subtropical marine boundary layer. Part I: Boundary-Layer Structure. *J.Atmos. Sci.*, 52, 2839-2868.

Kuettner, J. , 1959. The band structure of the atmosphere . *Tellus*, 11, 267-296.

Kuettner, J. P. , 1971. Cloud bands in the Earth's atmosphere. *Tellus*, 23, 4040-426.

Lamb, R. G., 1982. Diffusion in the convective boundary layer. In : Atmospheric Turbulence and Air Pollution Modelling. F.T.M. Nieuwstadt and H. van Dop, Eds. Reidel, Dordtrecht, Holland.Landau, L. D. and E. M. Lifshitz, 1944. Fluid Mechanics. English edn. Pergamon Press, London, 1959, 536 pp.

LeMone, M.A., 1990: Some observations of vertical velocity skewness in the planetary boundary layer. *J. Atmos. Sci*., 47, 1163-1169.

Lenschow, D.H., J.C.Wyngaard, W.T.Pennell, 1980: Mean-field and second-moment budgets in a baroclinic, convective boundary layer. *J. Atmos. Sci*., 37, 1313-1326.

Lock, A. P., and M. K. McVean, 1999: Parameterization of entrainment driven by surface heating and cloud-top cooling. *Quart. J. Roy. Meteorol. Soc*., 120,

Lilly, D.K., 1968: Models of cloud-capped mixed layers under a strong inversion. *Quart. J. Roy. Meteor. Soc.*., 94, 292-309.

Lutgens, F.K. and E.J. Tarbuck. 1995: The Atmosphere. Prentice-Hall, 462 pp.

McPherson, J.I., and A.K. Betts, 1995: Aircraft encounters with strong coherent vortices Over boreal forest. The Symposium on Boundary Layers and Turbulence. Charlotte, N.C., AMS, 424-427.

Mahrt, L., 1979: Penetrative convection at the top of a growing boundary layer. *Quart. J. Roy. Meteor. Soc.*., 105, 969-985.

Mason, P.J., 1989: Large-eddy simulation of the convective atmospheric boundary layer. *J.Atmos. Sci.*, 46, 1492-1516.

Misra, P.K., 1982: Dispersion of nonbuoyant particles inside a convective boundary layer. *Atmos. Envir*., 16, 239-243.

Moeng, C.-H., 1984: A large-eddy simulation model for the study of planetary boundary-layer turbulence. *J. Atmos. Sci.*, 41, 2052-3169.

Moeng C.-H. and U. Schumann, 1991: Composite structure of plumes in stratus-topped boundary layers. *J. Atmos. Sci*., 48, 2280-2291.

Moeng, C.-H., P.P.Sullivan, 1994: A comparison of shear- and buoyancy driven planetary boundary layer flows. *J. Atmos. Sci.*, 51, 999-1022.

Moeng, C.-H., 1998: Stratocumulus-topped atmospheric planetary boundary layer. In: *Buoyant Convection in Geophysical Flows*, NATO ASCI Series, vol 513, 421-440. Eds E.J. Plate, E.E.Fedorovich, D,X.Viegas and J.C. Wyngaard.

Moeng, C.-H., 1998: Stratocumulus-topped atmospheric planetary boundary layer. In: *Buoyant Convection in Geophysical Flows*, NATO ASCI Series, vol 513, 421-440. Eds E.J. Plate,

Monin, A.S., and A.M. Obukhov, 1954: Basic laws of turbulent mixing in the atmosphere near the ground. *Trans. Geof. Inst. Akad. Nauk USSR*, 151, 163-187.

Moninger, W.R., and R.A. Kropfli, 1982: Radar observations of a plume from an elevated continuous point source *J. Appl. Meteor*., 21, 11, 1685-1697

Moran, J.M. and M.D.Morgan, 1995: Essentials of Weather. Prentice-Hall, 351 pp.

Nichols S., and J. Leighton, 1986: An observational study of the structure of stratiform cloud sheets: Part I: Structure. *Q.J.R.Meteor. Soc*. 112, 431-460.

Nieuwstadt, F.T.M., 1984: The turbulent structure of the stable, nocturnal boundary layer. *J. Atmos. Sci* , 41, 2202-2216.

Nieuwstadt , F. T. M., P.J. Mason, C. H. Moeng, and U. Schumann, 1992: Large-eddy simulation of convective boundary-layer: A comparison of four computer codes. *Turbulent Shear Flows 8* (Eds. F. Durst, R. Friedrich, B.E.Launder, F.W. Schmidt, U. Schumann, and J.H.Whitelaw), Springer-Verlag, pp. 343-367.

Paluch I.R., and D.H. Lenchow, 1991: Stratiform cloud formation in the marine boundary layer. *J. Atmos. Sci*., 48, 2141-2158.

Panofsky, H.A., H. Tennekes, D.H. Lenschow, and J.C.Wyngaard, 1977: The characteristics of turbulent components in the surface layer under convective conditions. *Bound.-Layer Met*. 11, 355-361.

Pasquill, F. , 1961: The estimation of dispersion of windborne material. Meteor.Mag., 90, 33.

Pasquill, F. , 1974: Atmospheric Diffusion, J.Willey @ Sons.439 pp.

Plate, E.J. E.E. Fedorovich, D.X. Viegas, and J.C. Wyngaard , 1998: Buoyancy Convection in Geophysical Flows. NATO ASI Series, 491 pp.

Sawford, B.L., and F.M. Guest, 1987: Lagrangian stochastic analysis of flux-gradient relationships in the convective boundary layer. . *J. Atmos. Sci*., 44, 1152-1165.

Schemm, C. E., and F. B. Lipps, 1976: Some results from a simplified three-dimensional numerical model of atmospheric turbulence. *J. Atmos. Sci.*, 33, 1021-1041.

Schmidt, H., and U. Schumann, 1989: Coherent structure of the convective boundary layer derived from large-eddy simulation. *J. Fluid Mech*., 200, 511-562.

Siems S.T, C.S.Bretherton, M.B.Baker, S.S.Shy, and R.E.Breidenthal, 1990: Buoyancy reversal and cloud-top entrainment instability. *Q.J.R.Meteor.Soc*., 116, 705-739.

Sommeria, G., 1976, Three-dimensional simulation of turbulent processes in an undisturbed trade wind boundary layer. *J. Atmos. Sci.* , 33, 216-241.

Sorbjan, Z., 1986: On similarity in the atmospheric boundary layer. *Bound.-Layer Met*. 34,377-397.

Sorbjan, Z., 1988a: Structure of the stably-stratified boundary layer during the SESAME-1979 experiment. *Bound.-Layer Met*. 44, 255-266.

Sorbjan, Z., 1988 b: Local similarity of spectral and cospectral characteristics in the stable-continuous boundary layer. *Bound.-Layer Meteor.* , 35, 257-275.

Sorbjan, Z., 1989: Structure of the Atmospheric Boundary Layer. Prentice Hall, 317pp..

Sorbjan, Z., 1993: Monin-Obukhov similarity for refractive index revisited. *J. Atmos. Sci*., 50, 3677-3679.

Sorbjan, Z., 1995: Toward evaluation of heat fluxes in the convective boundary layer. *J. Appl. Meteor.* , 34, 1092-1098

Sorbjan, Z., 1995: Self-similar structure of the planetary boundary layer. In: The Planetary Boundary Layer and its Parameterizations. 1995 Summer Colloquium. NCAR. Boulder, Colorado, USA.

Sorbjan, Z., 1996a: Numerical study of penetrative and "solid lid" nonpenetrative convective boundary layers. J. Atmos. Sci., 53, 101-112.

Sorbjan, Z, 1996b: Effects caused by varying the strength of the capping inversion based on a large-eddy simulation model of the shear-free convective boundary layer. J. Atmos. Sci., 53, 2015-2024.

Sorbjan, Z., 1997: Decay of convective turbulence revisited. *Bound.-Layer Meteor*., 82, 501-515.

Sorbjan, Z., 1999a: Similarity of scalar fields in the convective boundary layer. *J. Atmos. Sci.,* 56, 2212-2221

Sorbjan, Z. and M.Uliasz, 1999b: Large-eddy simulation of air pollution dispersion in the nocturnal cloud-topped atmospheric boundary layer. *Bound.-Layer Meteor*., 91, 145-157.

Sorbjan, Z., 2001: An evaluation of local similarity on the top of the mixed layer based on large-eddy simulations. *Bound.-Layer Meteor.,* 101, 183-207.

Sorbjan, Z., 2003: Large-eddy simulation of the baroclinic mixed layer. *Bound.-Layer Meteor. (accepted).*

Stull, R.B.,1973: Inversion rise model based on penetrative convection. *J.Atmos. Sci,*, 30, 1092-1099.

Stull, R., 1976: The energetic of entrainment across a density interface. *J. Atmos. Sci.,* 33, 1260-1267.

Stull, R.B., 1988: An Introduction to Boundary Layer Meteorology. Kluwer Academic Publishers, 666 pp.

Sullivan, P.P., C.-H.Moeng, B, Stevens, D.H.Lenschow, and S.D.Mayor, 1998: Structure of the entrainment zone capping the convective boundary layer. *J.Atmos. Sci,* 55, 3042-3064.

Sun W.-Y., and Y. Ogura, 1980, Modeling the evolution of the convective planetary boundary layer. *J. Atmos. Sci.*, 37, 1558-1572.

Sun W.-Y., 1993. Numerical simulation of a planetary boundary layer: Part i: Cloud-freecase. *Beitr.Phys. Atmosph.*, 66, 3-16.

Telfort, J.W., and S.K. Chai, 1984: Inversion and fog, stratus and cumulus formation in warm air over cooler water. *Bound.-Layer Meteor.*, 29, 109-137.

Tennekes, H., 1973: A model for the dynamics of the inversion above a convective boundary layer. *J. Atmos. Sci.*, 30, 558-567.

Turton J., and S. Nicholls, 1987: A study of the diurnal variation of stratocumulus using a multiple mixed-layer model. *Q.J.R.Meteor. Soc*. 113, 969-1011.

Yamada, T., and G. Mellor, 1975: A simulation of the Wangara atmospheric boundary layer data. J. *Atmos. Sci.*, 32, 2309-2338.

Venkatram A. and J.C.Wyngaard (Eds), 1988. Lectures on Air Pollution Modelling. American Meteorological Society.,

Willis, G. E. and J. W. Deardorff, 1976. A laboratory study of dispersion from an elevated source in a convective mixed layer. *Atmos. Environ*., 12, 1305-1313.

Willis, G. E. and J. W. Deardorff, 1978. A laboratory study of diffusion into a convective planetary boundary layer. *Quart.J. R. Meteorol. Soc*., 105, 109-117.

Willis, G. E. and J. W. Deardorff, 1981. A laboratory study of dispersion from a source in the middle of the convective mixed layer. *Atmos. Environ*., 12, 1305-1313.

Wyngaard, J.C., O.R. Cote, and Y. Izumi, 1971: Local free convection, similarity, and the budgets of shear stress and heat flux. *J. Atmos. Sci*. 28, 1171-1182.

Wyngaard J. C., module. *J. Atmos. Sci*., 41, 1959-1969.

Wyngaard J.C., and R. A.Brost, 1984: Top-down and bottom-up diffusion in the convective boundary layer. *J. Atmos. Sci.*, 41, 102-112.

Wyngaard,1988: Advances and applications. In Flow and Transport in the Natural Environment. W.L. Steffen and O.T. Denmead (Eds.). Springer-Verlag, 384 pp.

Wyngaard, J. C. and O. R. Coté, K. S. Rao, 1974. Modelling the atmospheric boundary layer. *Adv. Geophys*., 18A, 193-211.

Zeman O., and J.L. Lumley, 1976: Modeling buoyancy driven mixed layers. *J. Atmos. Sci.*, 33, 1974-1988.

Zeman, O., and H. Tennekes, 1977: Parameterization of the turbulent energy budget at the top of the daytime atmospheric boundary layer. *J. Atmos. Sc*i., 34, 111-123.

Zilitinkievich, S.S., and D.V. Chalikov, 1968: On the computation of the vertical turbulent fluxes in the surface layer of the atmosphere from data of profile observations. *Izv. AN USSR*, ser. Fiz. Atmosph. i Okeana, 4, 915-929 (in Russian).